

BiMotion: B-spline Motion for Text-guided Dynamic 3D Character Generation

Miaowei Wang¹ Qingxuan Yan² Zhi Cao³ Yayuan Li³
Oisín Mac Aodha¹ Jason J. Corso³ Amir Vaxman¹

¹ University of Edinburgh ² Cornell University ³ University of Michigan

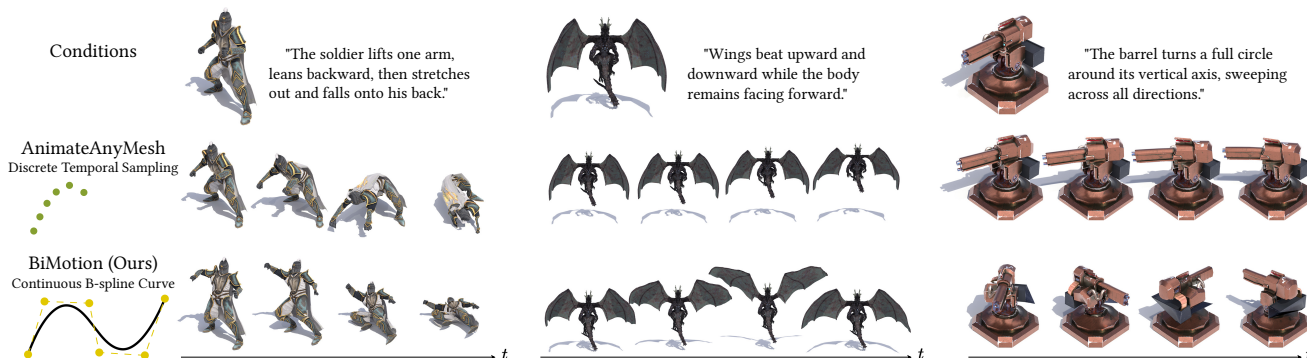


Figure 1. We propose **BiMotion**, a fast, feed-forward B-spline-based method for dynamic 3D character generation. It produces continuous, high-quality expressive motion trajectories aligned with rich textual prompts, outperforming discrete temporal sampling-based methods such as AnimateAnyMesh [101] under the same fixed-input constraint. See our project page for full motion dynamics.

Abstract

Text-guided dynamic 3D character generation has advanced rapidly, yet producing high-quality motion that faithfully reflects rich textual descriptions remains challenging. Existing methods tend to generate limited sub-actions or incoherent motion due to fixed-length temporal inputs and discrete frame-wise representations that fail to capture rich motion semantics. We address these limitations by representing motion with continuous differentiable B-spline curves, enabling more effective motion generation without modifying the capabilities of the underlying generative model. Specifically, our closed-form, Laplacian-regularized B-spline solver efficiently compresses variable-length motion sequences into compact representations with a fixed number of control points. Further, we introduce a normal-fusion strategy for input shape adherence along with correspondence-aware and local-rigidity losses for motion-restoration quality. To train our model, we collate BIMO, a new dataset containing diverse variable-length 3D motion sequences with rich, high-quality text annotations. Extensive evaluations show that our feed-forward framework BiMotion generates more expressive, higher-quality, and better prompt-aligned motions than existing state-of-the-art methods, while also achieving faster generation. Our project page is at: <https://wangmiaowei.github.io/BiMotion.github.io/>.

1. Introduction

Recent advances in content creation have shifted from static 3D generation [13, 102, 107, 124] toward dynamic 3D generation [62, 94, 100], driven by growing demands in gaming, film, and educational applications. Rather than simultaneously generating both geometry and motion [39, 41, 43, 76, 122], by decoupling motion generation from shape synthesis, recent methods [74, 96, 101, 116] focus solely on animating a given initial shape by leveraging existing 3D assets or mature generation models [64, 124]. This decoupling paradigm preserves subject consistency and enables direct use of existing 3D content libraries [10, 16, 27, 82, 91].

However, current feed-forward motion generation methods [101, 116, 122] face a critical limitation: they struggle to produce expressive, semantically complete motion that faithfully matches the user description (see Fig. 1). Existing methods typically employ VAE-latent diffusion models [77], with fixed-size inputs, forcing them to either crop motion sequences into short fragments [53, 101, 116] or uniformly downsample them [50, 122]. Cropping breaks motion completeness, capturing only isolated sub-actions like “rotate to the right” instead of the full user prompt (Fig. 1, Right). Temporal downsampling yields non-smooth, jittery results [122]. As a result, rich motion semantics present in variable-length datasets [22, 23, 52, 59], which contain motion spanning tens to hundreds of frames, are not captured.

The fundamental challenge is this: *how can variable-*

length, *semantically complete motions be represented within capacity-limited models that require fixed-size inputs?* Motion is inherently continuous, with frame count merely reflecting temporal sampling and semantic meaning (e.g., “a dragon flapping its wings”) is unchanged whether captured at 24 or 120 frames. Discrete frame-wise representation is hence a key bottleneck. Therefore, what is needed is a continuous, compact parameterization that preserves full motion semantics regardless of sequence length.

We introduce **BiMotion**, a B-spline-based motion representation that directly addresses this challenge. B-splines [8, 34] model continuous trajectories using a compact set of control points, providing exactly the parameterization we need. B-splines offer three properties ideal for representing motion: (1) continuity and differentiability for natural trajectories; (2) local controllability, where modifying one control point only affects its neighborhood; and (3) temporal reparameterization, allowing sampling at any time along a trajectory defined by control points. We further develop a closed-form, Laplacian-regularized B-spline solver that efficiently represents variable-length motion into fixed-size control point sets, preserving global motion semantics while maintaining continuous motion evolution.

Integrating B-spline control points into VAE-latent diffusion models as inputs requires rethinking how motion information is embedded. We propose a novel multi-level control-point embedding tailored for B-spline representation, which significantly outperforms standard frequency-based positional encodings [63] in motion reconstruction (Fig. 8). We also introduce a normal fusion strategy that enhances the VAE’s geometric awareness, effectively distinguishing closely positioned motion parts while remaining robust and efficient, unlike mesh-connectivity methods [101], which become unstable when scaled to many vertices. Our B-spline formulation enables projecting predicted control points back onto motion trajectories, supervised by a correspondence loss aligning with raw trajectory differences and a local rigidity loss preserving shape identity. To train BiMotion, we construct **BIMO**, a dataset comprising $\sim 39\text{K}$ sequences with control points, raw differences trajectory, and high-quality textual descriptions generated through a hybrid of human and automatic annotation with iterative feedback to ensure consistency and accuracy.

In summary, our main contributions are:

- BiMotion, a B-spline-based feed-forward framework that generates faster, more plausible, expressive, and semantically complete text-guided motion from an initial 3D shape than state-of-the-art methods (SOTAs).
- A specialized VAE with novel control-point embedding, normal fusion, and correspondence and rigidity losses tailored to B-spline motion representation.
- BIMO, a general dataset of $\sim 39\text{K}$ high-quality annotated motions represented by B-spline curves, and extensive ex-

periments validating our approach’s effectiveness.

2. Related Work

Static and Dynamic 3D Generation. Static and dynamic 3D generation methods follow similar technical trajectories. initial static approaches optimize shapes using image-generation models via Score Distillation Sampling (SDS) and its variants [69, 86, 98]. Dynamic 3D methods have used the same paradigm by extracting motion priors from video-generation models through video-based SDS variants [3, 51, 114]. As the Janus (multi-face) problem became evident [38, 99], subsequent works shifted to multi-view image diffusion [42, 55] and multi-view video diffusion [43, 71, 104, 117] to achieve view-consistent static [29, 56, 81, 125] and dynamic 3D generation [28, 39, 41, 76, 85, 100]. To mitigate geometry collapse and enable faster feed-forward generation, recent methods train directly on 3D assets instead of using multi-view projections [33, 105, 115, 123, 124]. The same paradigm has been applied to dynamic 3D generation [101, 116]. These models typically employ VAE-latent diffusion architectures that encode dynamic 3D assets into fixed-size latent spaces, which restricts variable-range motion awareness. Autoregressive models [88, 126] support variable-length sequences but are computationally expensive and struggle to generalize beyond human skeletons [68, 90, 103] for arbitrary character motion generation. To strike a balance, our work focuses on enabling a fixed-capacity model to support diverse, variable-length motions.

Conditional Motion Generation. Letting a user specify the desired motion—conditional generation—is essential for creating controllable, usable dynamic 3D assets in creative applications. Unconditional motion generation [7, 72, 122], however, does not support this rich need. Many works [12, 93, 97, 106, 116] target video-to-dynamic-3D generation because videos provide richer motion cues than text alone [11, 19, 37, 80, 101]. However, these methods are biased toward reconstruction from videos: generated motions can be sensitive to camera, content, and lighting changes [12, 110, 116], with quality largely dependent on the source video [113]. Some methods incorporate user-specified trajectories for finer control [2, 49, 60, 95]. Dynamic 3D generation can also be conditioned on the first and last frames [18, 78, 79], though this is closer to motion interpolation. Following [101], we condition motion generation on text and an initial 3D mesh, while our method remains adaptable to other conditioning inputs.

Motion Representation. In current dynamic 3D character pipelines, rigging, including skeletons and skinning, is essential for controlling shape deformation. Many works automatically estimate rigging [24, 32, 83, 121], which can drive motion generation by optimizing the skeleton using video [51, 51, 83]. Skeleton-based feed-forward ap-

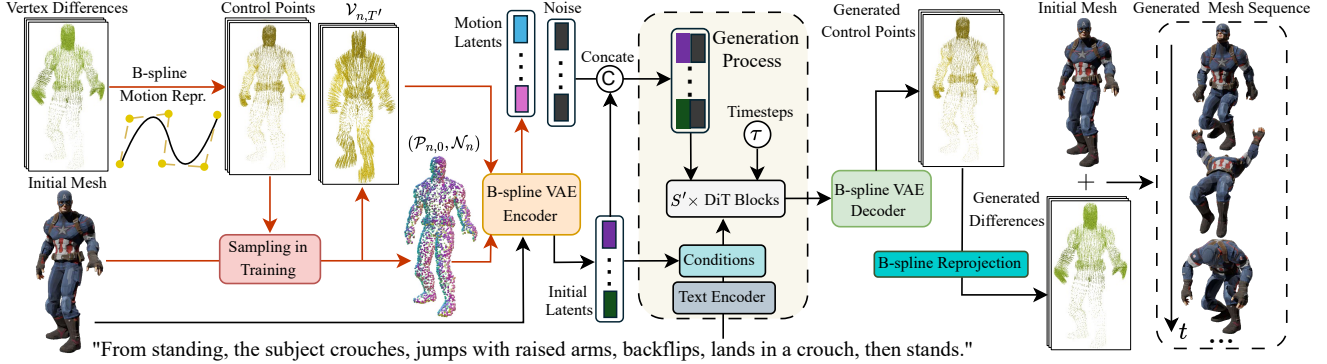


Figure 2. **Overview.** BiMotion uses a B-spline representation for motion generation. During training (red arrow), vertex differences are converted into control points and encoded into motion latents. During inference (black arrow), the initial mesh and the text prompt generate motion latents that are decoded into control points and converted into the generated mesh sequence via B-spline reprojection.

proaches are commonly used in human motion generation [15, 44, 48], but they typically require sequences padded to a predefined maximum length. Gat et al. [30] perform animal skeleton-driven motion generation, but still require a fixed number of skeleton joints, Zhang et al. [118] incorporate a physics engine to enhance elastic effects, and He et al. [35], Zhang et al. [119] learn rigging-like sparse handles from datasets to facilitate user-driven shape deformation. AnimateAnyMesh [101] learns motion tokens by sampling vertices, offering a potential route for universal feed-forward motion generation. However, these representations focus on shape deformation, with motion sequences still composed naively on a frame-by-frame basis. In contrast, we represent variable-length motion using B-spline curves. Splines [26] have long been used in geometric modeling [4, 31] and, more recently, in dynamic scene reconstruction [66, 84]. To our knowledge, we are the first to employ spline-based representations for motion generation.

3. Methodology

3.1. Problem Statement

Given a dataset of dynamic mesh sequences $\mathcal{D} = \{(M_{0:T}^{(i)}, y^{(i)})\}_{i=1}^N$, where each sequence $M_{0:T}$ has variable length $T + 1$, y is a user provided textual prompt, and N is the total number of sequences, our goal is to learn a θ -parameterized conditional posterior $p_{\theta}(M_{1:T} | M_0, y) \approx p_{\mathcal{D}}(M_{1:T} | M_0, y)$. At inference we wish to animate an initial mesh M_0 by sampling from $p_{\theta}(\cdot | M_0, y)$ conditioned on the user prompt y with the learned parameters θ . The initial mesh $M_0 = (\mathbf{V}_0, \mathbf{F}_0)$ contains vertex positions $\mathbf{V}_0 \in \mathbb{R}^{n_v \times 3}$ and shared triangular faces $\mathbf{F}_0 \in \mathbb{R}^{n_f \times 3}$ across all subsequent timesteps. To disentangle motion from shape, following [101, 116], we represent all subsequent frames by vertex-wise displacements $\{\mathbf{V}_t = \mathbf{V}_0 + \Delta \mathbf{V}_t\}_{t=1}^T$ via the initial vertex positions \mathbf{V}_0 and a vertex-wise difference $\Delta \mathbf{V}_t$. We stack vertex differences $\{\Delta \mathbf{V}_t\}_{t=1}^T$ into $\mathcal{V}_T \in \mathbb{R}^{T \times n_v \times 3}$.

3.2. Overview

We employ a VAE-latent diffusion approach for motion generation. During training, BiMotion (Fig. 2) first converts variable-length vertex differences \mathcal{V}_T into compact control points by representing each difference trajectory independently using B-splines. These control points are uniformly densely sampled, then randomly downsampled and encoded by a B-spline VAE encoder in each iteration to obtain motion latents. During inference (*i.e.*, motion generation), the model is conditioned on a text prompt y and an initial mesh M_0 , and transforms noise into motion latents. The VAE decoder then generates control points from these latents, which are reprojected into vertex differences of arbitrary length to generate the final 3D motion sequence. We describe the details of each stage below.

3.3. Preliminary: B-spline Curves

A 3D B-spline curve $\mathcal{C}(t)$ of degree d with k control points $\{\mathbf{p}_i \in \mathbb{R}^3\}_{i=0}^{k-1}$ is defined over the (time) parameter t [6] as:

$$\mathcal{C}(t) = \sum_{i=0}^{k-1} \mathcal{N}_{i,d}(t) \mathbf{p}_i, \quad t \in [u_d, u_{m-1-d}]. \quad (1)$$

The functions \mathcal{N} are local, with their support defined by a non-decreasing knot vector $\mathbf{u} = \{u_0, \dots, u_{m-1}\}$ satisfying $m = k + d + 1$. The basis functions $\{\mathcal{N}_{i,d}(t)\}_{i=0}^{k-1}$ are built by the Cox-de Boor recursion [21].

A *clamped* knot vector repeats the first and last knot values $d + 1$ times, *i.e.*, $u_0 = \dots = u_d$ and $u_{m-1-d} = \dots = u_{m-1}$, enforcing endpoint interpolation (Fig. 1, Left) $\mathcal{C}(u_d) = \mathbf{p}_0, \mathcal{C}(u_{m-1-d}) = \mathbf{p}_{k-1}$. With clamped ends and uniformly spaced interior knots, the curve attains C^{d-1} continuity at interior knots. Sampling the B-splines at timesteps t_1, \dots, t_T , we express the sampled points of Eq. (1) as:

$$\mathcal{C}_T = \mathcal{B}_{T,k} \mathcal{P}_k, \quad (2)$$

with the B-spline basis matrix $\mathcal{B}_{T,k} \in \mathbb{R}^{T \times k}$ stacked by

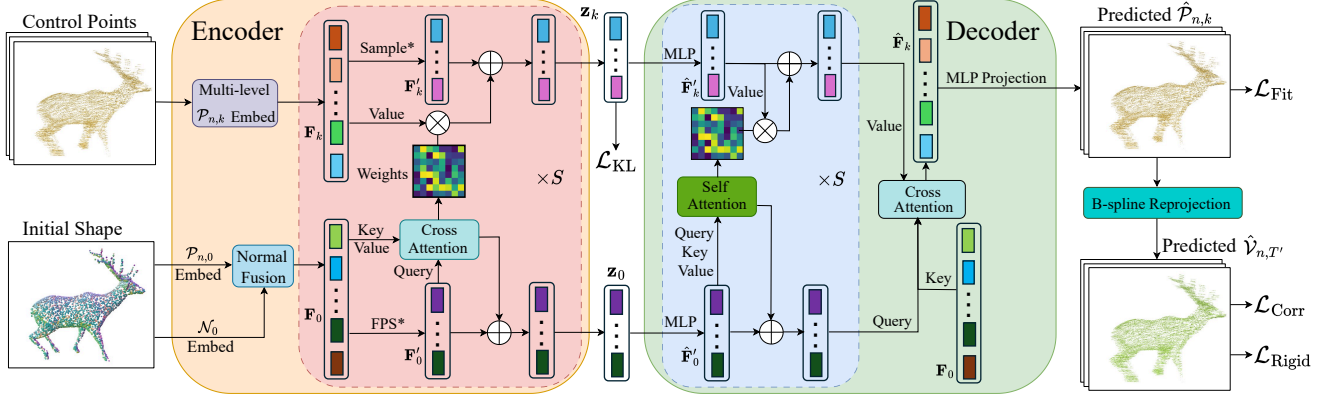


Figure 3. **B-spline VAE Pipeline.** Given the initial shape $(\mathcal{P}_{n,0}, \mathcal{N}_0)$ and control points $\mathcal{P}_{n,k}$, the *Encoder* compresses them into latent codes \mathbf{z}_0 and \mathbf{z}_k . The *Decoder* reconstructs the predicted control points $\hat{\mathcal{P}}_{n,k}$, which are then reprojected to point differences via the B-spline basis. Note, * indicates that \mathbf{F}'_k uses the FPS-sampled indices of \mathbf{F}_0 , \oplus denotes matrix addition, and \otimes denotes matrix multiplication.

rows $\{[\mathcal{N}_{0,d}(t), \dots, \mathcal{N}_{k-1,d}(t)]\}_{t=1}^T$ and the control-point matrix as $\mathcal{P}_k = [\mathbf{p}_0^\top; \dots; \mathbf{p}_{k-1}^\top] \in \mathbb{R}^{k \times 3}$.

3.4. B-spline Motion Representation

To obtain a fixed-size motion representation for variable- T sequence, the differences \mathcal{V}_T are approximated over time by the commonly used uniform cubic ($d = 3$) B-splines with stacked control points $\mathcal{P}_k \in \mathbb{R}^{k \times n_v \times 3}$, using least-squares fitting over temporal samples: $\min_{\mathcal{P}_k} \|\mathcal{B}_{T,k} \mathcal{P}_k - \mathcal{V}_T\|_F^2$.

When the number of control points $k \leq T$, the least-squares solution is unique. For short sequences where $k > T$, the system becomes underdetermined. To regularize this, we apply a Laplacian term that enforces natural transitions between adjacent control points. Let $\mathbf{L} \in \mathbb{R}^{k \times k}$ denote the discrete second-order difference operator. We then solve:

$$\min_{\mathcal{P}_k} \|\mathcal{B}_{T,k} \mathcal{P}_k - \mathcal{V}_T\|_F^2 + \mu \|\mathbf{L} \mathcal{P}_k\|_F^2, \quad (3)$$

which admits the closed-form solution [9]:

$$\mathcal{P}_k = (\mathcal{B}_{T,k}^\top \mathcal{B}_{T,k} + \mu \mathbf{L}^\top \mathbf{L})^{-1} \mathcal{B}_{T,k}^\top \mathcal{V}_T. \quad (4)$$

We denote the Laplacian-regularized least-square operator as $\mathcal{O}_{T,k} := (\mathcal{B}_{T,k}^\top \mathcal{B}_{T,k} + \mu \mathbf{L}^\top \mathbf{L})^{-1} \mathcal{B}_{T,k}^\top$ (see ablation in Fig. 6), which is efficiently computed via Cholesky decomposition [17], *i.e.*, under one second on a consumer-grade CPU for 200-frame mesh sequences with 50K vertices.

To train across the full spatial field and ensure robustness to varying mesh topologies (Fig. 10), following DNF [122], we uniformly pre-sample a dense set of $N = 200\text{K}$ points with normals \mathcal{N}_N from the initial mesh M_0 . The corresponding control points $\mathcal{P}_{N,k}$ of the B-splines $\mathcal{C}_N(t)$ and point differences $\mathcal{V}_{N,T}$ are efficiently barycentric interpolated from \mathcal{P}_k and \mathcal{V}_T , respectively. The $\mathcal{V}_{N,T}$ are temporally T' -uniformly sampled to $\mathcal{V}_{N,T'}$ for later training.

3.5. B-spline VAE

Following the above motion representation, we introduce a B-spline-based VAE architecture (see Fig. 3) to spatially

compress motion into compact latents for subsequent generative training. In each training iteration, we randomly downsample $n < N$ initial points $\mathcal{P}_{n,0} \in \mathbb{R}^{n \times 3}$ with normals $\mathcal{N}_n \in (\mathbb{S}^2)^n$ from the dense set in Sec. 3.4, and collect their corresponding control points $\mathcal{P}_{n,k} \in \mathbb{R}^{k \times n \times 3}$ and differences trajectory $\mathcal{V}_{n,T'} \in \mathbb{R}^{T' \times n \times 3}$. The initial shape and control points serve as inputs to the VAE. For the encoder, $\mathcal{P}_{n,0}$ provide absolute 3D coordinates, which are lifted using cosine positional encoding [63] and then projected via an MLP into c -dimensional point features $\mathbf{F}_{\mathcal{P}_0} \in \mathbb{R}^{n \times c}$.

Normal Fusion. The normals \mathcal{N} provide complementary local geometric cues, particularly where nearby points are far intrinsically on the mesh [75, 108]. We embed normals with a two-layer MLP to obtain $\mathbf{F}_{\mathcal{N}_0} \in \mathbb{R}^{n \times c}$ [112]. The normals are fused with the point features $\mathbf{F}_{\mathcal{P}_0}$ using a per-point cosine-similarity weight $w \in [0, 1]^n$ along the feature dimension, yielding the initial-shape embedding:

$$\mathbf{F}_0 = \mathbf{F}_{\mathcal{P}_0} + (w(\mathbf{F}_{\mathcal{P}_0}, \mathbf{F}_{\mathcal{N}_0}) \odot \mathbf{1}_c) \odot \mathbf{F}_{\mathcal{N}_0}, \quad (5)$$

where \odot denotes element-wise multiplication.

Control Point Embedding. Since conventional frequency encodings fail to capture the full motion patterns of control points (Fig. 8), we introduce a novel multi-level hierarchical embedding for $\mathcal{P}_{n,k}$, inspired by wavelet packet decomposition [89]. We denote a decreasing sequence of control-point counts as $[k_s, \dots, k_0]$ (from finer to coarser). The linear transport operator from coarse level k_{s-1} to fine level k_s is $\mathcal{T}_s = \mathcal{O}_{T',k_s} \mathcal{B}_{T',k_{s-1}} \in \mathbb{R}^{k_s \times k_{s-1}}$. A fine-level control points admits the decomposition interpolated from coarse level: $\mathcal{P}_{n,k_s} = \mathcal{T}_s \mathcal{P}_{n,k_{s-1}} + \mathcal{R}_s$, where the high-frequency residual is obtained: $\mathcal{R}_s = (I_{k_s} - \mathcal{T}_s \mathcal{T}_s^+) \mathcal{P}_{n,k_s}$, via the Moore–Penrose pseudo-inverse \mathcal{T}_s^+ . The residual from $\mathcal{P}_{n,k_{s-1}}$ to $\mathcal{P}_{n,k_{s-2}}$ is $\mathcal{R}_{s-1} = (I_{k_{s-1}} - \mathcal{T}_{s-1} \mathcal{T}_{s-1}^+) \mathcal{P}_{n,k_{s-1}} = [(I_{k_{s-1}} - \mathcal{T}_{s-1} \mathcal{T}_{s-1}^+) \mathcal{T}_s^+] \mathcal{P}_{n,k_s}$. Similarly, this proceeds recursively until \mathcal{R}_1 . The coarsest control points are derived by chained projection: $\mathcal{P}_{n,k_0} =$

$(\prod_{i=1}^s \mathcal{T}_i^+) \mathcal{P}_{n,k_s}$. Collecting all multilevel residuals and the coarsest coefficients forms the stacked embedding:

$$\mathcal{E}_k = [\mathcal{R}_s, \dots, \mathcal{R}_1, \mathcal{P}_{n,k_0}] = \mathcal{W}_k \mathcal{P}_{n,k_s}, \quad (6)$$

with the basis $\mathcal{W}_k \in \mathbb{R}^{(\sum_{i=0}^s k_i) \times k_s}$ registered as a buffer, \mathcal{E}_k is efficiently derived during training via a single matrix multiplication from \mathcal{P}_{n,k_s} padded by $\mathcal{P}_{n,k}$ (see Suppl.). To align with the feature dimension of \mathbf{F}_0 , the \mathcal{E}_k is passed through an MLP to obtain the motion embedding $\mathbf{F}'_k \in \mathbb{R}^{n \times c}$.

To compress the embeddings into fewer tokens $n' < n$, and following prior observations [35, 101, 120] that geometrically similar regions of the initial shape tend to exhibit similar motion patterns, we apply farthest point sampling (FPS) [70] to the normal-fused features \mathbf{F}_0 , producing a reduced set $\mathbf{F}'_0 \in \mathbb{R}^{n' \times c}$. The same sampling indices are then applied to each \mathbf{F}_k to obtain $\mathbf{F}'_k \in \mathbb{R}^{n' \times c}$. To capture long-range geometric correspondences, we adopt a cross-attention module that uses \mathbf{F}'_0 as the query, the full \mathbf{F}_0 as the key, and either \mathbf{F}_0 or \mathbf{F}_k as the value:

$$\begin{aligned} \mathbf{F}'_0 &= \text{CrossAttn}(\mathbf{F}'_0, \mathbf{F}_0, \mathbf{F}_0) + \mathbf{F}'_0, \\ \mathbf{F}'_k &= \text{CrossAttn}(\mathbf{F}'_0, \mathbf{F}_0, \mathbf{F}_k) + \mathbf{F}'_k. \end{aligned} \quad (7)$$

By stacking S such cross-attention layers, we alternately integrate global context into the sparse features \mathbf{F}'_0 and \mathbf{F}'_k , completing spatial compression for both the initial shape and motion. The compressed \mathbf{F}'_0 is projected by a single-layer MLP into the initial latent code \mathbf{z}_0 for conditional generation, while motion \mathbf{F}'_k is passed through two MLPs to predict the mean $\boldsymbol{\mu}_k$ and standard deviation $\boldsymbol{\sigma}_k$ respectively. The compact motion latent is then sampled as $\mathbf{z}_k = \boldsymbol{\mu}_k + \boldsymbol{\sigma}_k \cdot \epsilon$, $\epsilon \sim \mathcal{G}(0, 1)$, and $(\boldsymbol{\mu}_k, \boldsymbol{\sigma}_k)$ is regularized by the KL divergence \mathcal{L}_{KL} [45] to facilitate subsequent generation training. For the VAE decoder, $(\mathbf{z}_0, \mathbf{z}_k)$ are each reprojected by single-layer MLPs and processed by S alternating self-attention layers (cf. Eq. (7)) to recover FPS-sampled initial $\hat{\mathbf{F}}'_0$ and motion $\hat{\mathbf{F}}'_k$. To reconstruct the complete motion, we apply cross-attention with full initial feature $\hat{\mathbf{F}}'_0$ as query, sampled initial $\hat{\mathbf{F}}'_0$ as key, and sampled motion $\hat{\mathbf{F}}'_k$ as value:

$$\hat{\mathbf{F}}_k = \text{CrossAttn}(\hat{\mathbf{F}}'_0, \hat{\mathbf{F}}'_0, \hat{\mathbf{F}}'_k), \quad (8)$$

which then reconstructs the predicted control points $\hat{\mathcal{P}}_{n,k}$ via an MLP. For stable VAE training, we adopt the Charbonnier loss [5] to fit the input control points $\mathcal{P}_{n,k}$ as:

$$\mathcal{L}_{\text{Fit}} = \mathbb{E} \left[\sqrt{\|\hat{\mathcal{P}}_{n,k} - \mathcal{P}_{n,k}\|_F^2 + \delta^2} \right], \quad (9)$$

with $\delta = 1 \times 10^{-3}$ for numerical stability and smooth gradients. Besides, we introduce a correspondence loss to fit the GT sampled differences trajectory $\mathcal{V}_{n,T'}$ via B-spline re-projection from predicted control points $\hat{\mathcal{V}}_{n,T'} = \mathcal{B}_{T',k} \hat{\mathcal{P}}_{n,k}$:

$$\mathcal{L}_{\text{Corr}} = \mathbb{E} \left[\sqrt{\|\hat{\mathcal{V}}_{n,T'} - \mathcal{V}_{n,T'}\|_F^2 + \delta^2} \right], \quad (10)$$

with $T' = k = 16$ during training for comparability with [101]. Empirically, $\mathcal{L}_{\text{Corr}}$ decreases faster than \mathcal{L}_{Fit} , providing effective guidance during early training. We also introduce a local rigidity loss, inspired by skeletal representations, to enforce consistent local lengths across frames:

$$\mathcal{L}_{\text{Rigid}} = \mathbb{E} \left[\sqrt{(r_t(i, j) - r_{t-1}(i, j))^2 + \delta^2} \right], \quad (11)$$

where $r_t(i, j)$ denotes the L_2 motion distance from point i to its KNN neighbor j at time t , computed from $\hat{\mathcal{V}}_{n,T'}$. The total VAE training objective for parameters θ_{vae} is then:

$$\mathcal{L}_{\text{VAE}}(\theta_{\text{vae}}) = \mathcal{L}_{\text{Fit}} + \lambda_1 \mathcal{L}_{\text{Corr}} + \lambda_2 \mathcal{L}_{\text{Rigid}} + \lambda_3 \mathcal{L}_{\text{KL}}, \quad (12)$$

with weights $\lambda_1 = 3 \times 10^{-1}$, $\lambda_2 = 10^{-1}$ and $\lambda_3 = 2 \times 10^{-5}$.

3.6. Shape-Driven Text-to-Motion Generation

After the VAE encoding, we build a generative model conditioned (Fig. 2) on the initial shape and text to infer the motion latent distribution. To ensure stability, following [101, 116], we normalize the initial latent \mathbf{z}_0 and motion latent \mathbf{z}_k to $\tilde{\mathbf{z}}_0$ and $\tilde{\mathbf{z}}_k$ using their running means $(\tilde{\boldsymbol{\mu}}_0, \tilde{\boldsymbol{\mu}}_k)$ and standard deviations $(\tilde{\boldsymbol{\sigma}}_0, \tilde{\boldsymbol{\sigma}}_k)$ computed from the training set.

We employ rectified flow-matching (FM) transport, integrated from learnable velocity network $v_{\theta_{\text{vel}}}$ [57], to sample the normalized motion latent $\tilde{\mathbf{z}}_k$ at $\tau = 1$ from standard Gaussian noise ϵ at $\tau = 0$. The trajectory is defined as $\tilde{\mathbf{z}}_k^\tau = \tau \tilde{\mathbf{z}}_k + (1 - \tau) \epsilon$, $\tau \in [0, 1]$. With the initial $\tilde{\mathbf{z}}_0$ and textual prompt y as condition, the conditional velocity $v_{\theta_{\text{vel}}}(\tilde{\mathbf{z}}_k^\tau | \tau, \tilde{\mathbf{z}}_0, y)$ is trained with the following loss:

$$\mathcal{L}_{\text{FM}}(\theta_{\text{vel}}) = \mathbb{E} \|v_{\theta_{\text{vel}}}(\tilde{\mathbf{z}}_k^\tau | \tau, \tilde{\mathbf{z}}_0, y) - \mathbf{u}\|_F^2, \quad (13)$$

where the target velocity is $\mathbf{u} = \tilde{\mathbf{z}}_k - \epsilon$, and the sampling time τ follows a cosine schedule [25]. Following [101], the velocity network $v_{\theta_{\text{vel}}}$ is based on Diffusion Transformers (DiTs) [25, 67] with $S' = 12$ DiT blocks. To enhance spatial-motion correspondence, following Wan [92], $\tilde{\mathbf{z}}_0$ is concatenated with $\tilde{\mathbf{z}}_k^{(\tau)}$ as input and used together with text embeddings from the CLIP text encoder [73] as conditions via decoupled cross attention [111]. See Suppl. for details.

3.7. Sequence Generation at Inference

With the model parameters $\theta = (\theta_{\text{vae}}, \theta_{\text{vel}})$ trained, feed-forward inference can be performed. Given an initial mesh and text prompt, the initial latent \mathbf{z}_0 is computed via the VAE encoder with vertices and normals. A clean latent $\tilde{\mathbf{z}}_k$ is then sampled from noise ϵ via the flow-based ODE [14], applying classifier-free guidance with strength $\gamma = 3.0$, conditioned on the normalized initial latent $\tilde{\mathbf{z}}_0$ and text y . The original \mathbf{z}_k is restored using preserved statistics $(\tilde{\boldsymbol{\mu}}_k, \tilde{\boldsymbol{\sigma}}_k)$. The VAE decoder then predicts control points $\hat{\mathcal{P}}_k$ via the

normal-fused vertex feature \mathbf{F}_0 in Eq. (8). The generated vertex sequence is then obtained via B-spline reprojection:

$$\hat{\mathbf{V}}_{1:T} = \mathbf{V}_0 + \mathcal{B}_{T,k} \hat{\mathcal{P}}_k, \quad (14)$$

where the basis $\mathcal{B}_{T,k}$ can be built for any T , enabling mesh sequences of arbitrary length for broader applications.

4. Experiments

4.1. Dataset Preparation

To validate our method, we curated a new dataset called **BIMO**, comprising 38,944 motion sequences with a total of 3,682,790 frames. It integrates diverse mesh motion sequences from DeformingThings4D Animals [52], ObjaverseV1 [23], and ObjaverseXL [22]. Asset IDs from ObjaverseV1 were curated by Diffusion4D [53], while meta IDs from ObjaverseXL were filtered by GVFDiffusion [116]. We reserve 400 sequences for design validation. Each variable-length raw sequence from 5 to 200 frames, is converted into 16-frame B-spline control points following Sec. 3.4. For captions, DeformingThings4D provides human-annotated motion descriptions from OmniMotionGPT [109], with three captions per motion sequence. For Objaverse, we use an automatic captioning pipeline based on the multimodal VLM GPT-5, which generates three captions per rendered video in the style of DeformingThings4D. The pipeline includes a caption generator and an inspector to ensure correctness and consistency (see Suppl. for details). We will release BIMO upon acceptance.

4.2. Implementation Details

In Eq. (6), we support the simplest B-spline curves with $k_0 = 4$. Following [101] during training, we randomly downsample $n = 4096$ points which is further compressed into $n' = 512$ tokens, while the B-spline VAE employs an encoder with $S = 8$ cross-attention layers and a decoder with $S = 8$ self-attention layers. The VAE is optimized with Adam [58] using a learning rate of 1×10^{-4} with weight decay 0.01. The velocity field is trained with a learning rate of 1×10^{-5} , linearly warmed up from 0 over the first 1000 iterations. During generative training, following [101], we use a lightweight pre-trained CLIP ViT-L/14 [73] with a maximum text length of 77 for text embeddings, and we set a 0.1 dropout rate for both conditioning inputs. Both models apply random-noise and rotation augmentations to initial points, normals, points differences, and control points in each iteration. We use FP16 mixed precision and FlashAttention [20] to accelerate training. Both the VAE (Sec. 3.5) and the velocity network (Sec. 3.6) are trained on eight NVIDIA L40 GPUs for seven days.

4.3. Comparisons

Baselines. We compare against three SOTAs: (1) *AnimateAnyMesh* [101], the most related work, which performs

Table 1. **Quantitative Comparisons.** Our approach not only surpasses existing methods across multiple metrics (Sec. 4.3), but also requires less time and peak GPU memory (PG) on an A100 GPU.

Methods	VBench				
	OC \uparrow	SC \uparrow	TF \uparrow	AQ \uparrow	DD \uparrow
GVFDiffusion [116]	0.167	0.920	0.986	0.505	0.650
AnimateAnyMesh [101]	0.155	0.951	0.993	0.514	0.100
V2M4 [12]	0.175	0.876	0.986	0.478	0.750
BiMotion (Ours)	0.187	0.948	0.995	0.529	0.800

Methods	User Study			Efficiency	
	TA \uparrow	MP \uparrow	ME \uparrow	Time \downarrow	PG (GB) \downarrow
GVFDiffusion [116]	2.343	2.300	2.443	2.141m	14.057
AnimateAnyMesh [101]	2.314	2.686	2.443	16.847s	3.102
V2M4 [12]	2.876	2.714	3.048	1.672h	48.416
BiMotion (Ours)	4.095	4.062	4.048	4.383s	1.246

feed-forward generation from an initial mesh user-provided text prompt; (2) *GVFDiffusion* [116], which generates dynamic 3D Gaussians from videos; and (3) *V2M4* [12], which reconstructs dynamic meshes from monocular videos. To mitigate artifacts introduced during video preparation, we employ the high-quality video generator Kling [46] as the video source for the latter two methods.

Metrics. We evaluate on 20 randomly selected static meshes (twice the number used in AnimateAnyMesh), including AI-generated ones from Meshy [61] and existing assets without ground-truth motion. Following [43, 101], we render 16-frame animations from fixed viewpoints for fair comparison and assess perceptual metrics using VBench [40]: (1) *overall consistency* (OC) for prompt-video alignment, (2) *subject consistency* (SC) for appearance coherence, (3) *temporal flickering* (TF) for temporal stability, (4) *aesthetic quality* (AQ) for shape fidelity, and (5) *dynamic degree* (DD) for motion plausibility. We also report average generation time and peak GPU memory (PG) per mesh animation. To further evaluate motion quality, we conduct a **user study** with 20 participants. Each participant reviews 10 cases and rates each animation on a 5-point Likert scale (1 = Very Poor, 5 = Excellent) for three aspects: (1) *text-to-motion agreement* (TA), (2) *motion plausibility* (MP), and (3) *motion expressiveness* (ME). Final scores are averaged across all ratings (see Suppl. for details).

Results. In Fig. 4, SOTAs show clear limitations: the feed-forward GVFDiffusion often produces incorrect shapes or textures (*e.g.*, Tiger) and fails to reproduce desired motion patterns; AnimateAnyMesh yields only slight motion due to its small fixed-frame cropping during training, which cause higher subject consistency (which has inflated scores for near static video) but very low dynamic degree in Tab. 1. The optimization-based V2M4 is sensitive to video content and struggles to maintain object consistency across frames (*e.g.*, Robot and Tiger). Our method produces more accurate motions (*e.g.*, Moose) that better match text descriptions and contain fewer artifacts, thanks to efficient motion representation based on B-splines and high-quality annota-

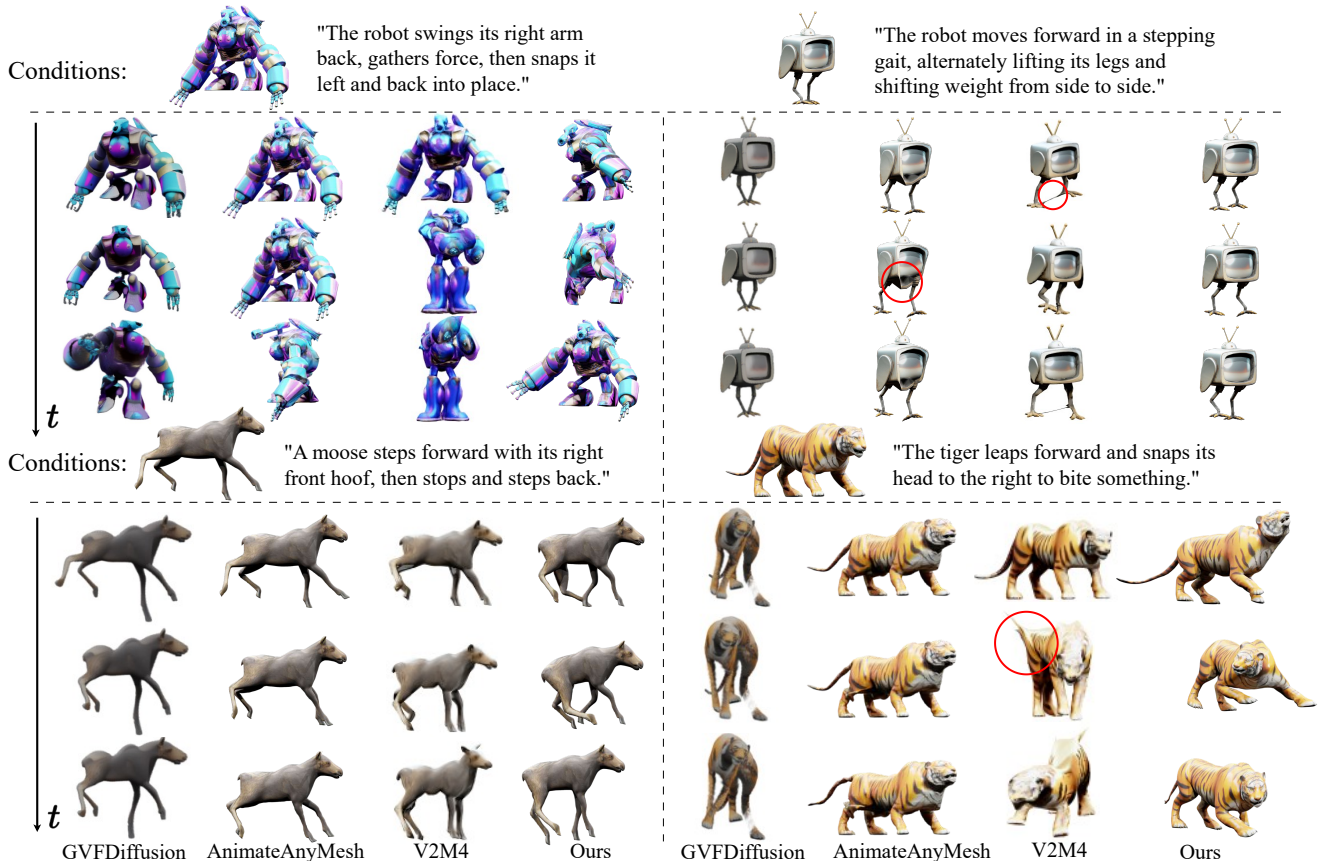


Figure 4. **Qualitative Comparisons.** Our method (BiMotion) results in superior motion quality and is more aligned with the user-provided text prompts. Artifacts for the baseline methods are highlighted in red. Please see the supplementary material for additional results.

tions during training. In Tab. 1, our approach outperforms in most Vbench metrics and achieves the highest scores across all user-study metrics, demonstrating better prompt–motion adherence and more expressive, plausibly coherent motion. Moreover, our method is more stable and efficient: as mesh vertices increase from 9K to 24K, AnimateAnyMesh’s generation time and peak GPU memory rise sharply from 6.4 s to 20.0 s and 1.6 GB to 3.6 GB due to heavy topology processing, whereas ours only slightly increase from 3.7 s to 4.6 s and 1.1 GB to 1.3 GB.

4.4. Ablations

B-spline Representation for Variable-length Sequences.

We encode variable-length motion sequences using B-splines and evaluate on the BIMO validation set (400 sequences of varying lengths). For fair comparison, the baselines uniformly downsample each sequence to 16 frames, the same number as our control points with the same VAE architecture, and linearly interpolate them back to the original length. In Tab. A1, all B-spline VAE variants achieve higher reconstruction fidelity than the linear interpolation baselines (first two rows). In Fig. 5, under the same 16-fixed VAE constraint, our method’s interpolations via Eq. (14) more faithfully reproduce the GT sequence, whereas the

Table 2. **VAE Quantitative Ablations.** “Rec Error” indicates the mean L1 error ($\times 10^{-2}$) averaged per trajectory and per instance.

B-Spline	NF	Control-PE	$\mathcal{L}_{\text{Corr}}$	$\mathcal{L}_{\text{Rigid}}$	Rec Error ↓
✗	✗	✗	✗	✗	3.237
✗	✓	✗	✓	✓	2.674
✓	✗	✓	✓	✓	1.328
✓	✓	✗	✓	✓	1.648
✓	✓	✓	✗	✓	1.303
✓	✓	✓	✓	✗	1.349
✓	✓	✓	✓	✓	1.078

baseline’s motion is inconsistent between the discrete samples, resulting in reconstruction failures. We further evaluate the proposed Laplacian regularization in Fig. 6, which produces more natural interpolations under fewer frames ($T < k$) compared to other regularization types, *e.g.*, Ridge.

Normal Fusion. Our normal fusion strategy (NF in Tab. A1) efficiently leverages local geometric cues from normals to distinguish spatially close but different motion units (Fig. 7). See the Suppl. for additional ablations.

Control Point Embedding. Our multi-level control-point embedding (Control-PE in Tab. A1) preserves both coarse and fine motion details better than the conventional frequency-based position encoding used in Ani-

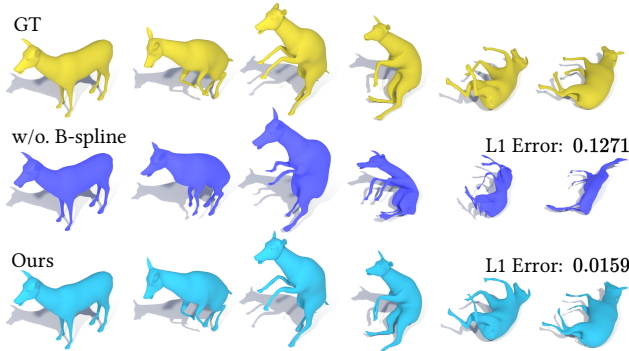


Figure 5. **B-spline Ablation.** B-spline interpolation from predicted control points achieves lower L1 error over the entire sequence than linear interpolation on sampled raw differences.



Figure 6. **Laplacian Regularizer L.** B-spline $\times 2$ interpolation comparison from a $T = 10$ mesh sequence comparing Ridge [36] and our Laplacian regularizer L. L produces more natural results.

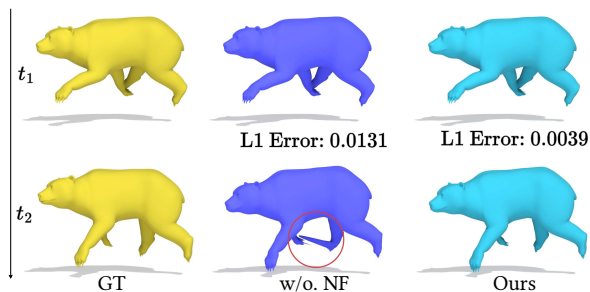


Figure 7. **Normal Fusion (NF) Ablation.** NF effectively separates nearby distinct parts. Without it, artifacts appear (see red).

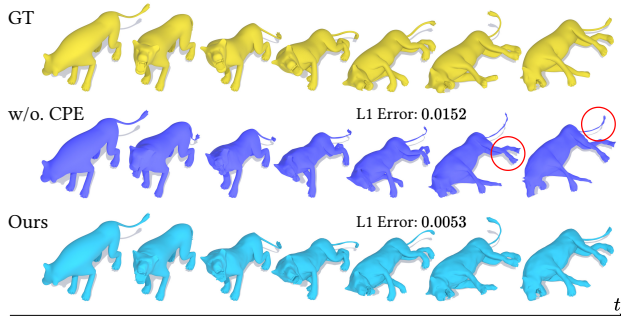


Figure 8. **Control-PE Ablation.** Our control-PE (Bottom) captures fine motion (e.g., the lion’s tail) and reduces artifacts (red circles) compared to conventional position encoding (Middle).

mateAnyMesh [101]. As shown in Fig. 8, Control-PE (Bottom) more accurately reproduces ground-truth motion (e.g., the lion’s tail).

Local Rigidity. We target mesh motion generation for 3D character animation, which inherently requires preserving local rigidity. The proposed local rigid loss $\mathcal{L}_{\text{Rigid}}$



Figure 9. $\mathcal{L}_{\text{Rigid}}$ Ablation. Our local rigid loss reduces the red-circled artifacts during motion generation. Prompt: “The pistol tilts up to an angled pose, then returns to forward-facing.”

(Eq. (11)) enforces piecewise consistency with the initial geometry across frames, helping retain shape identity during motion generation, as shown in Fig. 9.

Robustness to Meshing. Our dense-point training and normal fusion strategies are independent of fixed mesh topology, making our method robust to mesh changes (see Fig. 10) and capable of generating motion consistent with the user-provided input text, while AnimateAnyMesh fails.

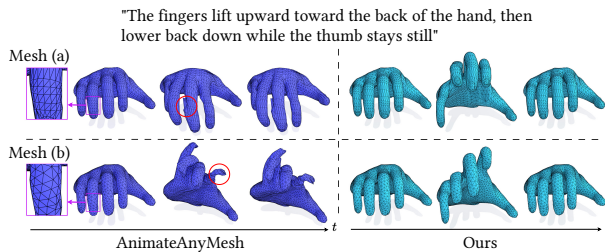


Figure 10. **Robustness to Meshing.** Ours produces consistent motion under mesh changes (Top to Bottom), whereas AnimateAnyMesh exhibits unstable motion and artifacts (red circles).

5. Discussion

Like all other generative tasks, improvements in motion generation depend on the availability of large and diverse dynamic sequences and sufficient compute. BiMotion nonetheless offers a complementary, staged contribution to character motion generation by demonstrating how to obtain continuous, compact, and efficient motion representations from variable-length sequences that can be used with constrained fixed-capacity models. This representation-centric view yields more expressive and plausible motions than SOTAs, and we expect these advantages to persist even as more powerful universal motion-generation models emerge. Extensive experiments and ablations verify the effectiveness of the proposed designs.

Limitations. BiMotion may fail to represent high-frequency details for very complex motions unless more control points are used. It also does not support topology-changing motion due to our fixed-mesh assumption.

BiMotion: B-spline Motion for Text-guided Dynamic 3D Character Generation

Supplementary Material

This supplementary material provides additional implementation details, further experiments and results, outlines the user study design and provides statistics, additional ablations (*e.g.*, extended normal-fusion ablations), and describes our dataset captioning pipeline. We also encourage readers to view the **accompanying video** for demonstrations of the dynamic results.

A. Additional Implementation Details

A.1. Velocity Network

We implement the velocity field $v_{\theta_{\text{vel}}}$ (described in Sec. 3.6 in the paper) based on Diffusion Transformer (DiTs) [67] (see Fig. A1). To promote spatial–motion correspondence, we follow the open-source image-to-video model Wan [92] to concatenate normalized latents along the channel dimension as $\tilde{\mathbf{z}}_{\parallel} = [\tilde{\mathbf{z}}_0, \tilde{\mathbf{z}}_{\mathcal{P}}^{(\tau)}]$. Text prompts are encoded using a pretrained CLIP text encoder [77] to obtain text embeddings. Following [25], we apply separate AdaLN [67] parameters conditioned on the timestep τ to modulate the concatenated latents, the latent $\tilde{\mathbf{z}}_0$, and the text embedding independently. The rescaled $\tilde{\mathbf{z}}_{\parallel}$ first passes through self-attention, then through cross-attention blocks that fuse information from the initial shape and the text embedding. This modality-specific AdaLN dynamically modulates each conditioning signal to vary modality-specific influence across sampling timesteps. After $S' = 12$ such DiT attention blocks, the network decodes the control-point velocities $v_{\theta_{\text{vel}}}(\tilde{\mathbf{z}}_{\mathcal{P}}^{(\tau)} | \tau, \tilde{\mathbf{z}}_0, y)$.

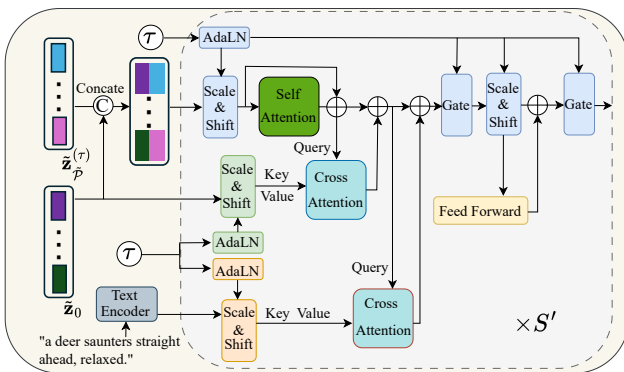


Figure A1. **Velocity Architecture.** The network $v_{\theta_{\text{vel}}}$ comprises S' stacked layers with self- and cross-attention modules.

A.2. Training Details

To reduce I/O cost during training, and to speed up training, each dense point set ($N = 200\text{K}$) is randomly

split into ten files of 20K points stored separately in pre-processing, where all initial shapes are normalized into range $[-0.9, 0.9]$. In our control-point embedding, we adopt a multi-level hierarchical strategy with a decreasing sequence (from finer to coarser) of control-point counts $[k_s, \dots, k_0] = [17, 15, 13, 11, 9, 7, 5, 4]$. When the input control-point sequence has length $k = 16$, we pad it to 17 by replicating the last control point to ensure compatibility.

B. Additional Experiments

B.1. Additional Comparisons

To provide a comprehensive comparison of mesh animation approaches, we include additional qualitative results against three baseline methods in Fig. A2. We further evaluate additional cases against the closest competitor, AnimateAnyMesh [101], using multi-mesh sources from Objaverse [23], Sketchfab [82], and AI-generated assets from Meshy [61] and Hunyuan3D [124]. Additional comparisons with AnimateAnyMesh are presented here in Fig. A3 and in Fig. 1 of the main paper. Across all settings, the results consistently support our main observation that method produces richer text-aligned motion, more natural dynamics, and more expressive animations compared to existing approaches.

For certain walking cases, such as Elephant and Robot in Fig. A3, the motion may appear to be “in-place.” This is because many dynamic 3D assets depict walking using in-place cycles by default. Artists typically add the global displacement (*i.e.*, the translation) only when integrating the character into a specific scene or environment.

B.2. Additional Baselines

Puppeteer. We also evaluate Puppeteer [83], a three-stage pipeline for driving the animation of a given mesh. First, it performs automatic rigging (skeleton and skinning estimation). Second, the static mesh is rendered to produce an initial conditioning frame for video generation. Third, it optimizes the frame-by-frame motion by driving the estimated skeleton, so that the rendered frames match Kling-generated video conditioned on the rendering and prompt [46]. As shown in Fig. A4, Puppeteer is sensitive to rigging quality. For example, an incorrect rig can cause the Spider sequence to remain static. In addition, Puppeteer easily accumulates errors from early frames during the optimization process, leading to severe artifacts in some cases, such as the Robot example. In our experiments, Puppeteer consumed a peak GPU memory of approximately 48 GB and required about 58 minutes of runtime on a single A100 GPU to process a



Figure A2. **Additional Qualitative Comparisons.** (a) GVFDiffusion [116], (b) AnimateAnyMesh [101], (c) V2M4 [12], (d) BiMotion (Ours). BiMotion yields more text-aligned, higher-quality motion. Visual artifacts are illustrated in red.

single sequence.

Video Generation Models. For comparison with video-based dynamic 3D generation methods [12, 116], we use Kling 2.1 [46] as the video source, conditioned on the first frame and the text prompts. To validate this choice, we

compare Kling with other state-of-the-art video generation models: Adobe Firefly [1], HunyuanVideo-I2V [47], and Wan-2.5 [92]. As shown in Fig. A5, Adobe Firefly and HunyuanVideo-I2V both struggle to maintain subject consistency and often introduce unrelated or unstable visual

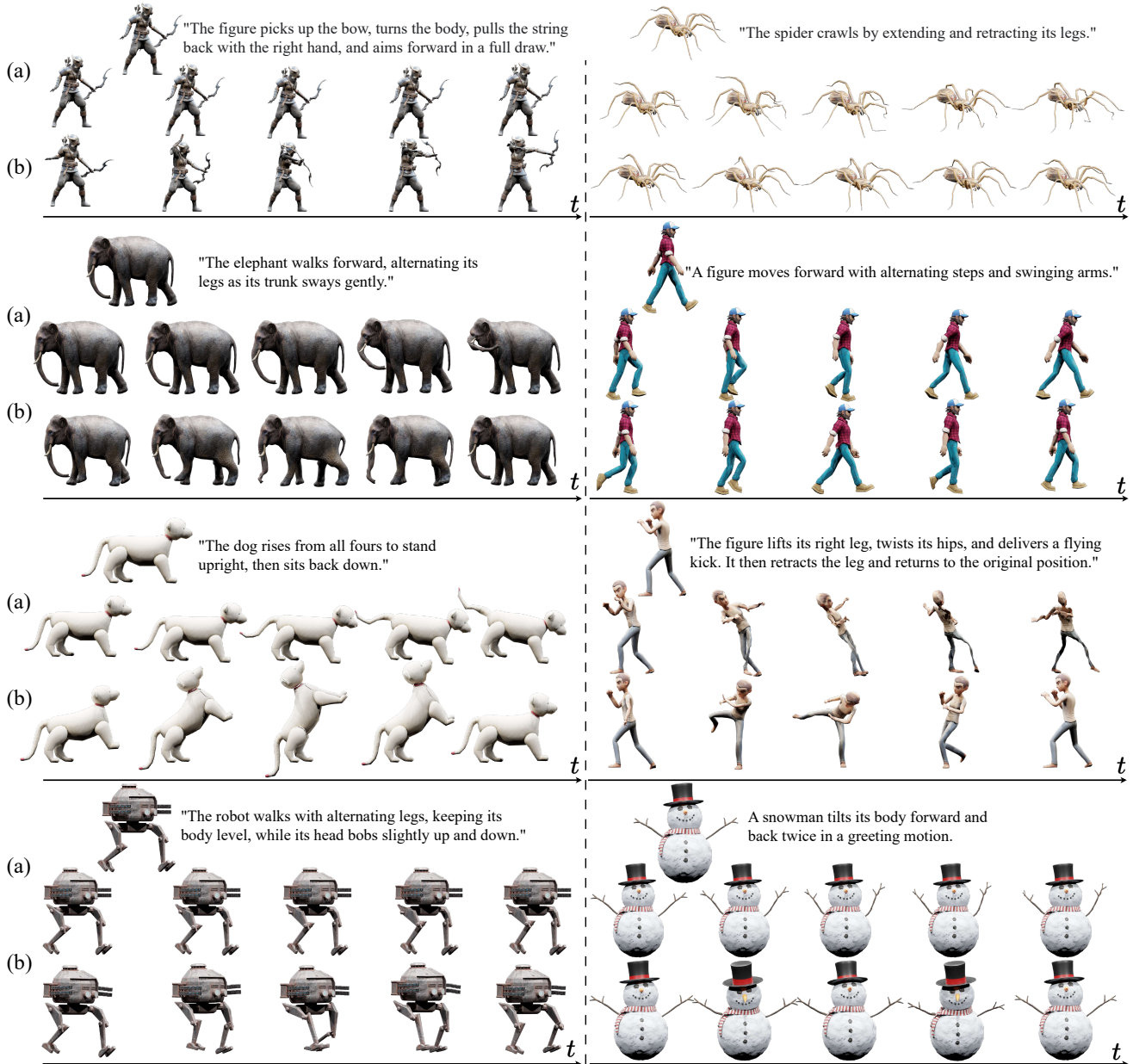


Figure A3. **Additional Qualitative Comparisons with AnimateAnyMesh.** (a) AnimateAnyMesh [101] and (b) BiMotion (Ours).

content. Wan-2.5 produces motion that aligns with the text prompts but lacks the expressiveness achieved by Kling.

B.3. Additional Ablations

Ablation of Number of Control Points. We use 16 control points in all experiments to remain consistent with our baselines (e.g., AnimateAnyMesh [101]). In new results in Tab. A1, on the DeformingThings4D split, we increase the number of control points yielding trajectories closer to the raw motion during preprocessing. However, more control points necessitates larger training cost.

Table A1. Ablation of the number of control points.

Number of control points	4	8	16	32
L2 Error ($\times 10^{-3}$) \downarrow	68.7	22.6	6.85	1.81

Variable-Length Sequence Representation. With BiMotion, the B-spline-based VAE robustly handles variable-length sequences, even with a limited number of control points. In addition to the mean statistics reported in Tab. 2 of the main paper, we provide binned reconstruction-error averages for a more fine-grained analysis. In Fig. A6 we re-

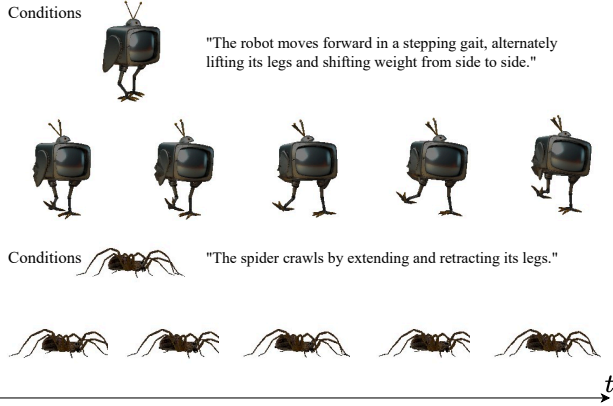


Figure A4. **Puppeteer Qualitative Results.** Results are rendered using the authors’ open-source renderer, whose texture appearance differs from ours and AnimateAnyMesh.

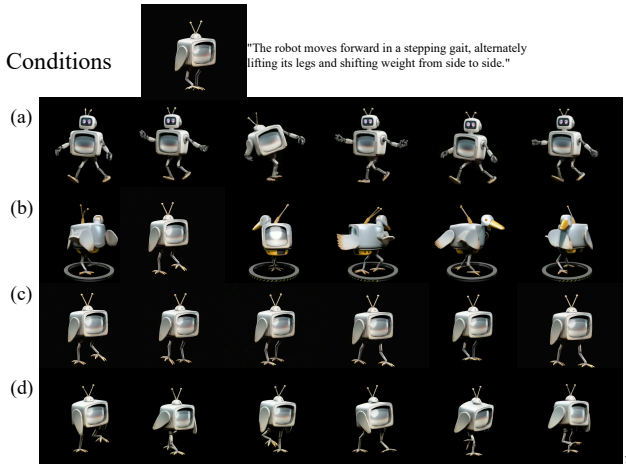


Figure A5. **Video Generation Model Comparison.** Qualitative comparison of video outputs from (a) Adobe Firefly [1], (b) HunyuanVideo-I2V [47], (c) Wan-2.5 [92], and (d) Kling 2.1 [46]. Note: these generation models convert transparent backgrounds to black by default.

port the mean L1 reconstruction error computed per trajectory and averaged per instance within each sequence-length bin. While our method reliably models short- and medium-length sequences, reconstruction error increases for longer sequences unless more than 16 control points are used. To ensure a fair comparison with AnimateAnyMesh, we fix the number of control points to 16 in all experiments.

Implicit Neural Representations (INRs). Recent studies (CanFields [96]) show that 4D INRs are computationally expensive due to per-frame marching cubes extraction and also struggle to maintain consistent mesh identity over time. In Fig. A7 we observe that the SOTA INR method DNF [122], produces noticeable artifacts. In contrast, our task focuses on animating existing static meshes with fixed

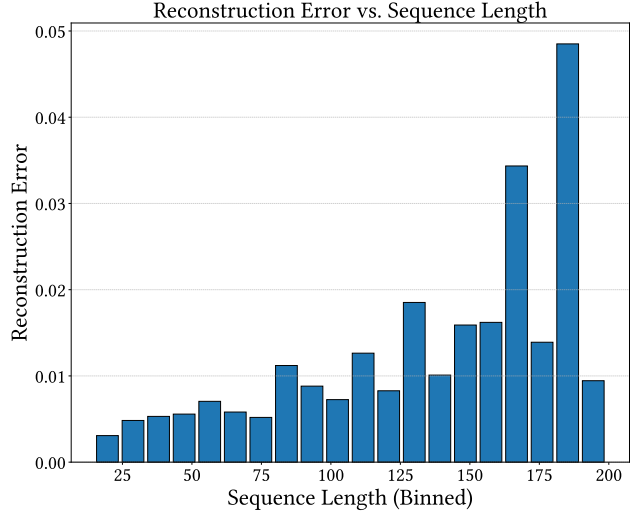


Figure A6. **VAE Reconstruction Error vs. Sequence Length.** Mean L1 reconstruction error for our VAE, computed per trajectory and averaged per instance, reported for each sequence-length bin.

topology, which is better aligned with modern animation pipelines and allows consistent texture preservation without re-mapping.



Figure A7. INR methods like DNF can introduce shape artifacts.

Additional Normal Fusion Ablations. We evaluate two alternative designs for incorporating surface normals into the initial shape features. (1) \mathcal{N}_0 **Frequency-PE.** Normals \mathcal{N} are encoded using the same frequency positional encoding (Frequency-PE) applied to the point coordinates [63] and then passed through an MLP to obtain $\mathbf{F}_{\mathcal{N}_0} \in \mathbb{R}^{n \times c}$. The fused feature \mathbf{F}_0 is computed using Eq. 5. (2) \mathcal{N}_0 **Concat.** As in the main paper, we first extract $\mathbf{F}_{\mathcal{N}_0}$ from \mathcal{N} using an MLP. To fuse normals, we concatenate $\mathbf{F}_{\mathcal{N}_0}$ with $\mathbf{F}_{\mathcal{P}_0}$ along the feature dimension and feed the result into another MLP to obtain \mathbf{F}_0 .

We report the VAE reconstruction error for these variants in Tab. A2. Encoding normals with Frequency-PE disrupts their spherical geometric structure, introducing noise and degrading reconstruction accuracy. In contrast, our cross-similarity fusion aligns the MLP-projected normal features to the same latent space as the 3D position features, enabling more effective fusion and yielding substantially improved reconstruction compared with naive concatenation.

B.4. User Study Details

We conducted an anonymous user study to evaluate the perceptual quality of text-driven mesh animations. A total of

Table A2. **Additional normal-fusion ablations.** Mean L1 reconstruction error ($\times 10^{-2}$), averaged per trajectory and per instance.

w/o \mathcal{N}_0	\mathcal{N}_0	Frequency-PE	\mathcal{N}_0 Concat.	Ours
1.328	1.331		1.294	1.078

20 participants with diverse levels of experience in computer vision and graphics were recruited. Each participant evaluated four generation methods on the same ten randomly selected example sequences and rated three criteria on a 5-point Likert scale (1 = Very Poor, 5 = Excellent). We evaluated the following three questions for each sequence: (i) *Text-to-Motion Agreement* (TA), (ii) *Motion Plausibility* (MP), and (iii) *Motion Expressiveness* (ME). In total, each participant contributed $4 \times 10 \times 3 = 120$ ratings.

Interface and Protocol. As shown in Fig. A8, for each example object, the form displayed a 2×2 grid of videos labeled Video 1–4, each corresponding to one of the four different methods. To avoid bias, the mapping from methods to Video 1–4 was anonymized and randomized per participant and per example. The physical positions of the four videos in the 2×2 grid were also randomly permuted for every page load. Participants could replay the clips freely before submitting their scores for TA/MP/ME (separate questions immediately under the grid). All responses were collected anonymously; participants could withdraw at any time without providing a reason. This study obtained ethics approval from the relevant internal ethics review board.

Results. We report both the mean and standard deviation for each method in Tab. A3. There we observe that users consistently favor BiMotion, which achieves the highest mean score and the lowest standard deviation across all metrics. For detailed data, please refer to the raw survey metadata in the accompanying supplementary material, titled “Anonymous User Study (Responses) – Form responses 1.csv”.

Table A3. **User study results.** Each cell shows the mean \pm standard deviation over all participants and examples.

Methods	TA \uparrow	MP \uparrow	ME \uparrow
GVFDiffusion [116]	2.343 \pm 0.407	2.300 \pm 0.380	2.443 \pm 0.387
AnimateAnyMesh [101]	2.314 \pm 0.394	2.686 \pm 0.464	2.443 \pm 0.357
V2M4 [12]	2.876 \pm 0.368	2.714 \pm 0.354	3.048 \pm 0.348
BiMotion (Ours)	4.095\pm0.334	4.062\pm0.328	4.048\pm0.339

C. Dataset and Preprocessing

C.1. Dataset Curation

To validate our method, we curated **BIMO** (Bspline Motion) dataset. We collect diverse mesh motion sequences from multiple datasets: DeformingThings4D [52], ObjaverseV1 [23], and ObjaverseXL [22]. For DeformingTh-

ings4D, we use the official script to extract animal mesh sequences from the raw ‘.anime’ files. For ObjaverseV1 and ObjaverseXL, we extract sequences with more than ten frames, discarding low-motion sequences based on object-center displacement, and bounding-box scale changes. We handle multiple raw formats from Objaverse (e.g., “.glb”, “.gltf”, “.fbx”) and filter out unnecessary elements such as “icosphere”, “sphere”, “proxy”, “env”, “origin”, “pivot”, “camera”, “ground”, “floor”, and “light”. The ObjaverseV1 asset IDs are curated by Diffusion4D [53], while ObjaverseXL meta IDs are filtered by GVFDiffusion [116]. All mesh sequences are capped at 200 frames following AnimateAnyMesh [101]. The distribution of mesh sequence lengths is illustrated in Fig. A10, and the summary statistics of our curated dataset are presented in Tab. A4. The final dataset comprises 38,944 motion sequences with a total of 3,682,790 frames.

Table A4. **Dataset statistics.** Summary statistics of our curated mesh motion dataset **BIMO**.

Dataset Source	Number of Motions	Total Frames
DeformingThings4D [52]	1,770	87,052
ObjaverseV1 [23]	10,550	1,116,134
ObjaverseXL [22]	26,624	2,479,604
Total motions	38,944	3,682,790

C.2. Auto-Captioning Pipeline

To obtain captions for conditioning our model, we use human-annotated motion descriptions provided by OmniMotionGPT [109] for DeformingThings4D, where each motion is annotated with three captions written by trained annotators. For Objaverse, there are no captions available, and so we build an automatic captioning pipeline (see Fig. A9) designed to emulate the style of the DeformingThings4D annotations. To reduce LLM token usage, we adopt a hyper-prompt design that first summarizes human annotations with an LLM to produce three concise prompts for a VLM. These distilled prompts, paired with the rendered frames, are supplied to the VLM as an alternative to requiring expensive to obtain human annotations for each caption. Concretely, we prompt an LLM (GPT-5 [65]) to imitate human annotators and generate three distinct video-captioning prompts. Our initial hyper-prompt that is provided to the LLM is:

Hyper Prompt

The following examples show how real human annotators describe the motion observed in a given sequence of dynamic frames:

Case 1 A bear stands up and then returns to all

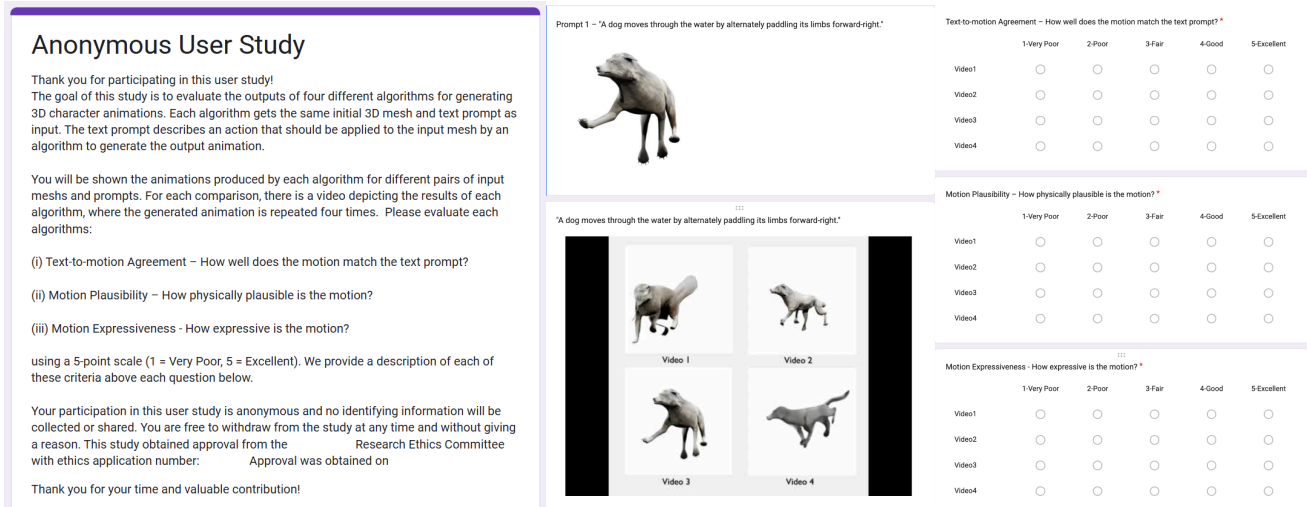


Figure A8. **User Study Interface and Protocol.** **Left:** Instructions page. Screenshot of the questionnaire introduction; personal or institutional information approved by the research ethics committee has been masked. **Middle:** Video comparison interface showing the conditions of both the first frame and the textual prompt, along with four videos generated by four randomly ordered methods. **Right:** Three evaluation questions used to collect user preferences, forming the basis of the subjective evaluation metrics.

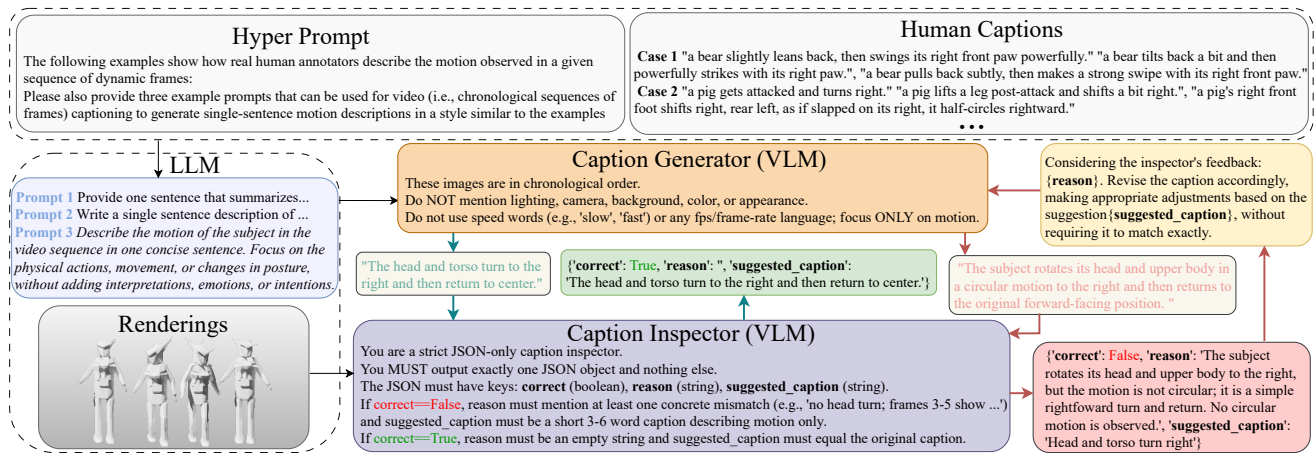


Figure A9. **Auto-captioning pipeline.** We propose an iterative captioning pipeline that incorporates both a caption inspector and a caption generator to produce accurate and consistent captions for dynamic assets.

fours. Another description states that the bear pushes with its front paws, stands on its hind legs, and then settles back down. A third annotator writes that the bear rose to its feet, used its front paws for support, stood upright, and then rested.

Case 2 A bull makes a left turn while remaining in one spot in the water. Another description notes that the bull turns in place, while a third says the bull swims in circles in the water.

Case 3 A wolf retreats in fright. Another annotator writes that the wolf withdraws in fear, while a third notes that the wolf is startled on the left and retreats to the right.

Case 4 A wolf falls into the water and moves forward. Another version describes it as dropping into the water, while a third says it plunges into the water and relaxes.

Case 5 A deer falls from above downward. Another description states that the deer descends from a

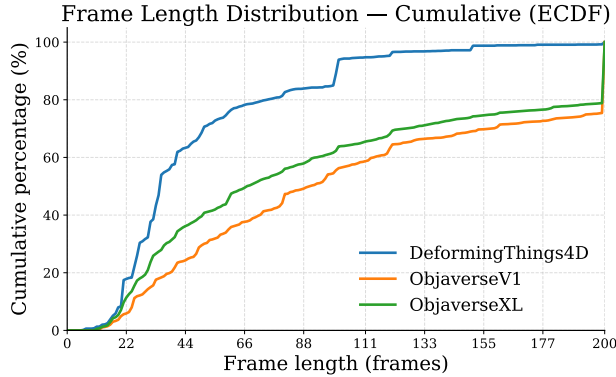


Figure A10. **Frame-length cumulative distribution.** Distribution of mesh sequence lengths (length ≤ 200) from DeformingThings4D [52], ObjaverseV1 [23], and ObjaverseXL [22].

higher to a lower position, while a third says it drops from high to low.

Case 6 A deer swims to the left while staying in place. Another annotator describes it as paddling left without advancing, while a third writes that it moves left in the water without forward motion.

Please also provide three example prompts that can be used for video (*i.e.*, chronological sequences of frames) captioning to generate single-sentence motion descriptions in a style similar to the examples above.

Given the above hyper-prompt, we obtain the following three auto-captioning prompts from the LLM which concisely summarizes the original hyper-prompt:

LLM Generated Prompt

1. Describe the motion of the subject in the video sequence in one concise sentence. Focus on the physical actions, movement, or changes in posture, without adding interpretations, emotions, or intentions.
2. Write a single-sentence description of what the subject does in the given sequence of frames. Include details about direction, movement, or interactions with the environment, but remain objective and observable.
3. Provide one sentence that summarizes the main motion occurring in the video. Describe only what is visually happening, such as movement, turning, rising, falling, or swimming, in chronological order.

Next, we render the Objaverse dynamic assets from a fixed front-view camera using a modified Blender script adapted from Diffusion4D [53]. Rendering is performed on ten A6000 GPUs with the Cycles engine, producing transparent 256×256 frames. We then use a VLM (GPT-5) to generate captions for each rendered sequence. To ensure consistency and reliability, we incorporate an iterative caption-inspection loop using the same model. The caption inspector (implemented with the same VLM GPT-5) receives both the renderings and the captions produced by the caption generator, evaluates their correctness, and provides reasoning and suggested revisions when necessary. The caption-generation agent then updates the caption and repeats the process six times until the inspector approves.

C.3. VLM Ablations



GPT-5: "The fox stays on its feet and turns its head side-to-side, alternating between left and right from a central position."

Qwen-2.5: "The fox turns its head to the right, then rotates its entire body to face left while taking a step forward."

LLaVa: "The fox in the video sequence is seen walking, running, and jumping in a wooded area."



GPT-5: "The articulated robotic arm lifts and extends its segments, swinging the forearm outward to the right while rotating the end effector into a tilted orientation."

Qwen-2.5: "The robotic arm extends its jointed segments outward, rotating and adjusting its position to reach a specific point in space."

LLaVa: "The robot arm moves from a horizontal position to a vertical position, then back to horizontal, and finally to a vertical position again in a sequence of frames."

Figure A11. **VLM Captioning Ablation.** We compare captions generated by three video–language models (VLMs). Using GPT-5 produces concise and motion-faithful descriptions closely aligned with the real 4D dynamics.

To validate our VLM choice, we ablate GPT-5, Qwen-2.5 [87], and LLaVA-NeXT-Video [54] in Fig. A11. GPT-5 consistently yields motion-focused, non-speculative descriptions that match the DeformingThings4D annotation style. Qwen-2.5 frequently hallucinates global behaviors (*e.g.*, stepping forward, full-body reorientation) and conflates pose with inferred intent. LLaVA-NeXT-Video more often attributes locomotion or complex actions absent from the frames. These errors shift the caption distribution away from true 4D motion and weaken text–motion correspondence during training. Our GPT-5 hyper-prompt pipeline produces stable, grounded, and fine-grained captions that improve the robustness and fidelity of downstream text-conditioned animation synthesis.

References

- [1] Adobe. Free ai video generator: Text to video online – adobe firefly, 2025. 10, 12
- [2] Sherwin Bahmani, Xian Liu, Wang Yifan, Ivan Skorokhodov, Victor Rong, Ziwei Liu, Xihui Liu, Jeong Joon Park, Sergey Tulyakov, Gordon Wetzstein, et al. Tc4d: Trajectory-conditioned text-to-4d generation. In *European Conference on Computer Vision*, 2024. 2
- [3] Sherwin Bahmani, Ivan Skorokhodov, Victor Rong, Gordon Wetzstein, Leonidas Guibas, Peter Wonka, Sergey Tulyakov, Jeong Joon Park, Andrea Tagliasacchi, and David B. Lindell. 4d-fy: Text-to-4d generation using hybrid score distillation sampling. *Computer Vision and Pattern Recognition*, 2024. 2
- [4] Chandrjit L Bajaj. Splines and geometric modeling. In *Handbook of discrete and computational geometry*. 2017. 3
- [5] Jonathan T Barron. A general and adaptive robust loss function. In *Computer Vision and Pattern Recognition*, 2019. 5
- [6] Richard H Bartels, John C Beatty, and Brian A Barsky. *An introduction to splines for use in computer graphics and geometric modeling*. Morgan Kaufmann, 1995. 3
- [7] David Björkstrand, Tiesheng Wang, Lars Bretzner, and Josephine Sullivan. Unconditional human motion and shape generation via balanced score-based diffusion. *arXiv:2510.12537*, 2025. 2
- [8] Javier Bonet and Richard D Wood. *Nonlinear continuum mechanics for finite element analysis*. Cambridge university press, 1997. 2
- [9] D. Calvetti, S. Morigi, L. Reichel, and F. Sgallari. Tikhonov regularization and the l-curve for large discrete ill-posed problems. *Journal of Computational and Applied Mathematics*, 2000. Numerical Analysis 2000. Vol. III: Linear Algebra. 4
- [10] CGTrader. Cgtrader free 3d models. <https://www.cgtrader.com/free-3d-models>. Accessed: 2025-11-08. 1
- [11] Ce Chen, Shaoli Huang, Xuelin Chen, Guangyi Chen, Xiaoguang Han, Kun Zhang, and Mingming Gong. Ct4d: Consistent text-to-4d generation with animatable meshes. *arXiv:2408.08342*, 2024. 2
- [12] Jianqi Chen, Biao Zhang, Xiangjun Tang, and Peter Wonka. V2m4: 4d mesh animation reconstruction from a single monocular video. In *International Conference on Computer Vision*, 2025. 2, 6, 10, 13
- [13] Minghao Chen, Roman Shapovalov, Iro Laina, Tom Monnier, Jianyuan Wang, David Novotny, and Andrea Vedaldi. Partgen: Part-level 3d generation and reconstruction with multi-view diffusion models. In *Computer Vision and Pattern Recognition*, 2025. 1
- [14] Ricky T. Q. Chen. torchdiffeq, 2018. 5
- [15] Zedong Chu, Feng Xiong, Meiduo Liu, Jinzhi Zhang, Mingqi Shao, Zhaoxu Sun, Di Wang, and Mu Xu. Humanrig: Learning automatic rigging for humanoid character in a large scale dataset. In *Computer Vision and Pattern Recognition*, 2025. 3
- [16] ClaraIO. Clara.io 3d library. <https://clara.io/library>. Accessed: 2025-11-08. 1
- [17] PyTorch Contributors. torch.linalg.cholesky. Accessed: 2025-10-17. 4
- [18] Luca Cosmo, Antonio Norelli, Oshri Halimi, Ron Kimmel, and Emanuele Rodola. Limp: Learning latent shape representations with metric preservation priors. In *European conference on computer vision*, 2020. 2
- [19] Sisi Dai, Xinxin Su, Boyan Wan, Ruizhen Hu, and Kai Xu. Textmesh4d: High-quality text-to-4d mesh generation. *arXiv:2506.24121*, 2025. 2
- [20] Tri Dao. FlashAttention-2: Faster attention with better parallelism and work partitioning. In *International Conference on Learning Representations*, 2024. 6
- [21] Carl De Boor. *A Practical Guide to Splines*. Springer, 1978. 3
- [22] Matt Deitke, Ruoshi Liu, Matthew Wallingford, Huong Ngo, Oscar Michel, Aditya Kusupati, Alan Fan, Christian Laforte, Vikram Voleti, Samir Yitzhak Gadre, et al. Objaverse-xl: A universe of 10m+ 3d objects. *Advances in Neural Information Processing Systems*, 2023. 1, 6, 13, 15
- [23] Matt Deitke, Dustin Schwenk, Jordi Salvador, Luca Weihs, Oscar Michel, Eli VanderBilt, Ludwig Schmidt, Kiana Ehsani, Aniruddha Kembhavi, and Ali Farhadi. Objaverse: A universe of annotated 3d objects. In *Computer Vision and pattern recognition*, 2023. 1, 6, 9, 13, 15
- [24] Yufan Deng, Yuhao Zhang, Chen Geng, Shangzhe Wu, and Jiajun Wu. Anymate: A dataset and baselines for learning 3d object rigging. In *SIGGRAPH*, 2025. 2
- [25] Patrick Esser, Sumith Kulal, Andreas Blattmann, Rahim Entezari, Jonas Müller, Harry Saini, Yam Levi, Dominik Lorenz, Axel Sauer, Frederic Boesel, et al. Scaling rectified flow transformers for high-resolution image synthesis. In *International Conference on Machine Learning*, 2024. 5, 9
- [26] David R Forsey and Richard H Bartels. Hierarchical b-spline refinement. In *Computer graphics and interactive techniques*, 1988. 3
- [27] Free3D. Free3d models. <https://free3d.com/3d-models/>. Accessed: 2025-11-08. 1
- [28] Junyao Gao, Jiaying Li, Wenran Liu, Yanhong Zeng, Fei Shen, Kai Chen, Yanan Sun, and Cairong Zhao. Character-shot: Controllable and consistent 4d character animation. *arXiv:2508.07409*, 2025. 2
- [29] Ruiqi Gao, Aleksander Hołyński, Philipp Henzler, Arthur Brussee, Ricardo Martin-Brualla, Pratul Srinivasan, Jonathan T Barron, and Ben Poole. Cat3d: create anything in 3d with multi-view diffusion models. In *Advances in Neural Information Processing Systems*, 2024. 2
- [30] Inbar Gat, Sigal Raab, Guy Tevet, Yuval Reshef, Amit Haim Bermano, and Daniel Cohen-Or. Anytop: Character animation diffusion with any topology. In *SIGGRAPH*, 2025. 3
- [31] Shufei Ge, Shijia Wang, and Lloyd Elliott. Shape modeling with spline partitions. *Statistics and Computing*, 2023. 3
- [32] Zhiyang Guo, Jinxu Xiang, Kai Ma, Wengang Zhou, Houqiang Li, and Ran Zhang. Make-it-animatable: An effi-

- cient framework for authoring animation-ready 3d characters. In *Computer Vision and Pattern Recognition*, 2025. 2
- [33] Junlin Han, Jianyuan Wang, Andrea Vedaldi, Philip Torr, and Filippos Kokkinos. Flex3d: Feed-forward 3d generation with flexible reconstruction model and input view curation. In *International Conference on Machine Learning*, 2024. 2
- [34] H Haron, A Rehman, DIS Adi, SP Lim, and T Saba. Parameterization method on b-spline curve. *Mathematical Problems in Engineering*, 2012. 2
- [35] Guangzhao He, Chen Geng, Shangzhe Wu, and Jiajun Wu. Category-agnostic neural object rigging. In *Computer Vision and Pattern Recognition*, 2025. 3, 5
- [36] Arthur E Hoerl and Robert W Kennard. Ridge regression: Biased estimation for nonorthogonal problems. *Technometrics*, 12(1):55–67, 1970. 8
- [37] Fangzhou Hong, Mingyuan Zhang, Liang Pan, Zhongang Cai, Lei Yang, and Ziwei Liu. Avatarclip: zero-shot text-driven generation and animation of 3d avatars. *Transactions on Graphics*, 2022. 2
- [38] Susung Hong, Donghoon Ahn, and Seungryong Kim. Debiasing scores and prompts of 2d diffusion for view-consistent text-to-3d generation. *Neural Information Processing Systems*, 2023. 2
- [39] Hanzhuo Huang, Yuan Liu, Ge Zheng, Jiepeng Wang, Zhiyang Dou, and Sibeil Yang. Mvtokenflow: High-quality 4d content generation using multiview token flow. In *International Conference on Learning Representations*, 2025. 1, 2
- [40] Ziqi Huang, Yinan He, Jiashuo Yu, Fan Zhang, Chenyang Si, Yuming Jiang, Yuanhan Zhang, Tianxing Wu, Qingyang Jin, Nattapol Chanpaisit, Yaohui Wang, Xinyuan Chen, Limin Wang, Dahua Lin, Yu Qiao, and Ziwei Liu. VBench: Comprehensive benchmark suite for video generative models. In *Computer Vision and Pattern Recognition*, 2024. 6
- [41] Zehuan Huang, Haoran Feng, Yangtian Sun, Yuanchen Guo, Yanpei Cao, and Lu Sheng. Animax: Animating the inanimate in 3d with joint video-pose diffusion models. *arXiv:2506.19851*, 2025. 1, 2
- [42] Zehuan Huang, Yuan-Chen Guo, Haoran Wang, Ran Yi, Lizhuang Ma, Yan-Pei Cao, and Lu Sheng. Mv-adapter: Multi-view consistent image generation made easy. In *International Conference on Computer Vision*, 2025. 2
- [43] Yanqin Jiang, Chaohui Yu, Chenjie Cao, Fan Wang, Weiming Hu, and Jin Gao. Animate3d: Animating any 3d model with multi-view video diffusion. *Advances in Neural Information Processing Systems*, 2024. 1, 2, 6
- [44] Aliasghar Khani, Arianna Rampini, Evan Atherton, and Bruno Roy. Unimogen: Universal motion generation. *arXiv:2505.21837*, 2025. 3
- [45] Diederik P. Kingma and Max Welling. Auto-encoding variational bayes. In *International Conference on Learning Representations*, 2014. 5
- [46] Kling AI. Kling ai: Next-generation ai creative studio. <https://klingai.com/>, 2024. Accessed: 2024-02-05, 07, 01, 04. 6, 9, 10, 12
- [47] Weijie Kong, Qi Tian, Zijian Zhang, Rox Min, Zuozhuo Dai, Jin Zhou, Jiangfeng Xiong, Xin Li, Bo Wu, Jianwei Zhang, et al. Hunyuanvideo: A systematic framework for large video generative models. *arXiv:2412.03603*, 2024. 10, 12
- [48] Jiefeng Li, Jinkun Cao, Haotian Zhang, Davis Rempe, Jan Kautz, Umar Iqbal, and Ye Yuan. Genmo: Generative models for human motion synthesis. In *International Conference on Computer Vision*, 2025. 3
- [49] Ruining Li, Chuanxia Zheng, Christian Rupprecht, and Andrea Vedaldi. Puppet-master: Scaling interactive video generation as a motion prior for part-level dynamics. In *International Conference on Computer Vision*, 2025. 2
- [50] Ruining Li, Chuanxia Zheng, Christian Rupprecht, and Andrea Vedaldi. Puppet-master: Scaling interactive video generation as a motion prior for part-level dynamics. In *International Conference on Computer Vision*, 2025. 1
- [51] Xuan Li, Qianli Ma, Tsung-Yi Lin, Yongxin Chen, Chenfanfu Jiang, Ming-Yu Liu, and Donglai Xiang. Articulated kinematics distillation from video diffusion models. In *Computer Vision and Pattern Recognition*, 2025. 2
- [52] Yang Li, Hikari Takehara, Takafumi Taketomi, Bo Zheng, and Matthias Nießner. 4dcomplete: Non-rigid motion estimation beyond the observable surface. *International Conference on Computer Vision*, 2021. 1, 6, 13, 15
- [53] Hanwen Liang, Yuyang Yin, Dejia Xu, Hanxue Liang, Zhangyang Wang, Konstantinos N Plataniotis, Yao Zhao, and Yunchao Wei. Diffusion4d: fast spatial-temporal consistent 4d generation via video diffusion models. In *Advances in Neural Information Processing Systems*, 2024. 1, 6, 13, 15
- [54] Haotian Liu, Yuheng Li, Zhuowan Zhang, and Chunyuan Li. LLaVA-NeXT-Video: Video Large Multimodal Models, 2024. 15
- [55] Minghua Liu, Chao Xu, Haian Jin, Linghao Chen, Mukund Varma T, Zexiang Xu, and Hao Su. One-2-3-45: Any single image to 3d mesh in 45 seconds without per-shape optimization. *Advances in Neural Information Processing Systems*, 2023. 2
- [56] Minghua Liu, Ruoxi Shi, Linghao Chen, Zhuoyang Zhang, Chao Xu, Xinyue Wei, Hansheng Chen, Chong Zeng, Jiayuan Gu, and Hao Su. One-2-3-45++: Fast single image to 3d objects with consistent multi-view generation and 3d diffusion. In *Computer Vision and Pattern Recognition*, 2024. 2
- [57] Xingchao Liu, Chengyue Gong, et al. Flow straight and fast: Learning to generate and transfer data with rectified flow. In *International Conference on Learning Representations*, 2023. 5
- [58] Ilya Loshchilov and Frank Hutter. Decoupled weight decay regularization. In *International Conference on Learning Representations*, 2017. 6
- [59] Qianli Ma, Jinlong Yang, Anurag Ranjan, Sergi Pujades, Gerard Pons-Moll, Siyu Tang, and Michael J. Black. Learning to Dress 3D People in Generative Clothing. In *Computer Vision and Pattern Recognition*, 2020. 1
- [60] Jiageng Mao, Boyi Li, Boris Ivanovic, Yuxiao Chen, Yan Wang, Yurong You, Chaowei Xiao, Danfei Xu, Marco

- Pavone, and Yue Wang. Dreamdrive: Generative 4d scene modeling from street view images. In *International Conference on Robotics and Automation*, 2025. 2
- [61] Meshy. Discover — meshy. <https://www.meshy.ai/discover>, 2025. Accessed: 2025-10-27. 6, 9
- [62] Qiaowei Miao, Kehan Li, Jinsheng Quan, Zhiyuan Min, Shaojie Ma, Yichao Xu, Yi Yang, Ping Liu, and Yawei Luo. Advances in 4d generation: A survey. *arXiv:2503.14501*, 2025. 1
- [63] Ben Mildenhall, Pratul P Srinivasan, Matthew Tancik, Jonathan T Barron, Ravi Ramamoorthi, and Ren Ng. Nerf: Representing scenes as neural radiance fields for view synthesis. *Communications of the ACM*, 2021. 2, 4, 12
- [64] Weizhi Nie, Ruidong Chen, Weijie Wang, Bruno Lepri, and Nicu Sebe. T2td: Text-3d generation model based on prior knowledge guidance. *Pattern Analysis and Machine Intelligence*, 2025. 1
- [65] OpenAI. Introducing GPT-5, 2025. Accessed: 2025-11-03. 13
- [66] Jongmin Park, Minh-Quan Viet Bui, Juan Luis Gonzalez Bello, Jaeho Moon, Jihyong Oh, and Munchurl Kim. Splines: Robust motion-adaptive spline for real-time dynamic 3d gaussians from monocular video. In *Computer Vision and Pattern Recognition*, 2025. 3
- [67] William Peebles and Saining Xie. Scalable diffusion models with transformers. In *International Conference on Computer Vision*, 2023. 5, 9
- [68] Ekkasit Pinyoanuntapong, Muhammad Usama Saleem, Pu Wang, Minwoo Lee, Srijan Das, and Chen Chen. Bamm: Bidirectional autoregressive motion model. In *European Conference on Computer Vision*, 2024. 2
- [69] Ben Poole, Ajay Jain, Jonathan T Barron, and Ben Mildenhall. Dreamfusion: Text-to-3d using 2d diffusion. In *International Conference on Learning Representations*, 2023. 2
- [70] Charles Ruizhongtai Qi, Li Yi, Hao Su, and Leonidas J Guibas. Pointnet++: Deep hierarchical feature learning on point sets in a metric space. *Advances in Neural Information Processing Systems*, 2017. 5
- [71] Hao Qin, Luyuan Chen, Ming Kong, Mengxu Lu, and Qiang Zhu. Distilling multi-view diffusion models into 3d generators. *arXiv:2504.00457*, 2025. 2
- [72] Sigal Raab, Inbal Leibovitch, Peizhuo Li, Kfir Aberman, Olga Sorkine-Hornung, and Daniel Cohen-Or. Modi: Unconditional motion synthesis from diverse data. In *Computer Vision and Pattern Recognition*, 2023. 2
- [73] Alec Radford, Jong Wook Kim, Chris Hallacy, Aditya Ramesh, Gabriel Goh, Sandhini Agarwal, Girish Sastry, Amanda Askell, Pamela Mishkin, Jack Clark, et al. Learning transferable visual models from natural language supervision. In *International Conference on Machine Learning*, 2021. 5, 6
- [74] Ohad Rahamim, Ori Malca, Dvir Samuel, and Gal Chechik. Bringing objects to life: 4d generation from 3d objects. *arXiv:2412.20422*, 2024. 1
- [75] Haoxi Ran, Jun Liu, and Chengjie Wang. Surface representation for point clouds. In *Computer Vision and Pattern Recognition*, 2022. 4
- [76] Jiawei Ren, Cheng Xie, Ashkan Mirzaei, Karsten Kreis, Ziwei Liu, Antonio Torralba, Sanja Fidler, Seung Wook Kim, Huan Ling, et al. L4gm: Large 4d gaussian reconstruction model. *Advances in Neural Information Processing Systems*, 2024. 1, 2
- [77] Robin Rombach, Andreas Blattmann, Dominik Lorenz, Patrick Esser, and Björn Ommer. High-resolution image synthesis with latent diffusion models. In *Computer Vision and Pattern Recognition*, 2022. 1, 9
- [78] Lu Sang, Zehranaz Canfes, Dongliang Cao, Riccardo Marin, Florian Bernard, and Daniel Cremers. 4deform: Neural surface deformation for robust shape interpolation. In *Computer Vision and Pattern Recognition*, 2025. 2
- [79] Lu Sang, Zehranaz Canfes, Dongliang Cao, Riccardo Marin, Florian Bernard, and Daniel Cremers. Twosquared: 4d generation from 2d image pairs. In *International Conference on 3D Vision*, 2025. 2
- [80] Ruizhi Shao, Jingxiang Sun, Cheng Peng, Zerong Zheng, Boyao Zhou, Hongwen Zhang, and Yebin Liu. Control4d: Efficient 4d portrait editing with text. In *Proceedings of the IEEE/CVF Conference on Computer Vision and Pattern Recognition (CVPR)*, pages 4556–4567, 2024. 2
- [81] Yichun Shi, Peng Wang, Jianglong Ye, Long Mai, Kejie Li, and Xiao Yang. Mvdream: Multi-view diffusion for 3d generation. In *International Conference on Learning Representations*, 2023. 2
- [82] Sketchfab. Sketchfab free 3d models. <https://sketchfab.com/features/free-3d-models>. Accessed: 2025-11-08. 1, 9
- [83] Chaoyue Song, Xiu Li, Fan Yang, Zhongcong Xu, Jiacheng Wei, Fayao Liu, Jiashi Feng, Guosheng Lin, and Jianfeng Zhang. Puppeteer: Rig and animate your 3d models. In *Advances in Neural Information Processing Systems*, 2025. 2, 9
- [84] Mingyang Song, Yang Zhang, Marko Mihajlovic, Siyu Tang, Markus Gross, and Tunç Ozan Aydın. Spline deformation field. In *SIGGRAPH*, 2025. 3
- [85] Qi Sun, Zhiyang Guo, Ziyu Wan, Jing Nathan Yan, Shengming Yin, Wengang Zhou, Jing Liao, and Houqiang Li. Eg4d: Explicit generation of 4d object without score distillation. In *International Conference on Representation Learning*, 2025. 2
- [86] Boshi Tang, Jianan Wang, Zhiyong Wu, and Lei Zhang. Stable score distillation for high-quality 3d generation. *arXiv:2312.09305*, 2023. 2
- [87] Qwen Team. Qwen2.5: A scalable and open large language model family, 2024. 15
- [88] Keyu Tian, Yi Jiang, Zehuan Yuan, Bingyue Peng, and Liwei Wang. Visual autoregressive modeling: Scalable image generation via next-scale prediction. *Advances in neural information processing systems*, 2024. 2
- [89] Wu Ting, Yan Guo-Zheng, Yang Bang-Hua, and Sun Hong. Eeg feature extraction based on wavelet packet decomposition for brain computer interface. *Measurement*, 2008. 4
- [90] Linnan Tu, Lingwei Meng, Zongyi Li, Hefei Ling, and Shijuan Huang. Autoregressive motion generation with gaussian mixture-guided latent sampling. In *Advances in Neural Information Processing Systems*, 2025. 2

- [91] TurboSquid. Turbosquid free 3d models. <https://www.turbosquid.com/Search/3D-Models/free>. Accessed: 2025-11-08. 1
- [92] Team Wan, Ang Wang, Baole Ai, Bin Wen, Chaojie Mao, Chen-Wei Xie, Di Chen, Feiwu Yu, Haiming Zhao, Jianxiao Yang, et al. Wan: Open and advanced large-scale video generative models. *arXiv:2503.20314*, 2025. 5, 9, 10, 12
- [93] Chaoyang Wang, Ashkan Mirzaei, Vidit Goel, Willi Menapace, Aliaksandr Siarohin, Michael Vasilkovsky, Ivan Skorokhodov, Vladislav Shakhrai, Sergei Korolev, Sergey Tulyakov, et al. Fused view-time attention and feedforward reconstruction for 4d scene generation. In *Advances in Neural Information Processing Systems*, 2025. 2
- [94] Chaoyang Wang, Peiye Zhuang, Tuan Duc Ngo, Willi Menapace, Aliaksandr Siarohin, Michael Vasilkovsky, Ivan Skorokhodov, Sergey Tulyakov, Peter Wonka, and Hsin-Ying Lee. 4real-video: Learning generalizable photorealistic 4d video diffusion. In *Computer Vision and Pattern Recognition*, 2025. 1
- [95] Lening Wang, Wenzhao Zheng, Yilong Ren, Han Jiang, Zhiyong Cui, Haiyang Yu, and Jiwen Lu. Occsora: 4d occupancy generation models as world simulators for autonomous driving. *arXiv:2405.20337*, 2024. 2
- [96] Miaowei Wang, Changjiang Li, and Amir Vaxman. Can-fields: Consolidating diffeomorphic flows for non-rigid 4d interpolation from arbitrary-length sequences. In *International Conference on Computer Vision*, 2025. 1, 12
- [97] Yikai Wang, Xinzhou Wang, Zilong Chen, Zhengyi Wang, Fuchun Sun, and Jun Zhu. Vidu4d: Single generated video to high-fidelity 4d reconstruction with dynamic gaussian surfels. *Advances in Neural Information Processing Systems*, 2024. 2
- [98] Zhengyi Wang, Cheng Lu, Yikai Wang, Fan Bao, Chongxuan Li, Hang Su, and Jun Zhu. Prolificdreamer: High-fidelity and diverse text-to-3d generation with variational score distillation. *Advances in neural information processing systems*, 2023. 2
- [99] Yujie Wei, Shiwei Zhang, Zhiwu Qing, Hangjie Yuan, Zhiheng Liu, Yu Liu, Yingya Zhang, Jingren Zhou, and Hongming Shan. Dreamvideo: Composing your dream videos with customized subject and motion. In *Computer Vision and Pattern Recognition*, 2024. 2
- [100] Rundi Wu, Ruiqi Gao, Ben Poole, Alex Trevithick, Changxi Zheng, Jonathan T Barron, and Aleksander Holynski. Cat4d: Create anything in 4d with multi-view video diffusion models. In *Computer Vision and Pattern Recognition*, 2025. 1, 2
- [101] Zijie Wu, Chaohui Yu, Fan Wang, and Xiang Bai. Animateanymesh: A feed-forward 4d foundation model for text-driven universal mesh animation. In *International Conference on Computer Vision*, 2025. 1, 2, 3, 5, 6, 8, 9, 10, 11, 13
- [102] Jianfeng Xiang, Zelong Lv, Sicheng Xu, Yu Deng, Ruicheng Wang, Bowen Zhang, Dong Chen, Xin Tong, and Jiaolong Yang. Structured 3d latents for scalable and versatile 3d generation. In *Computer Vision and Pattern Recognition*, 2025. 1
- [103] Lixing Xiao, Shunlin Lu, Huaijin Pi, Ke Fan, Liang Pan, Yueer Zhou, Ziyong Feng, Xiaowei Zhou, Sida Peng, and Jingbo Wang. Motionstreamer: Streaming motion generation via diffusion-based autoregressive model in causal latent space. *arXiv:2503.15451*, 2025. 2
- [104] Kevin Xie, Amirmojtaba Sabour, Jiahui Huang, Despoina Paschalidou, Greg Klar, Umar Iqbal, Sanja Fidler, and Xiaoahui Zeng. Videopanda: Video panoramic diffusion with multi-view attention. *arXiv:2504.11389*, 2025. 2
- [105] Bojun Xiong, Si-Tong Wei, Xin-Yang Zheng, Yan-Pei Cao, Zhouhui Lian, and Peng-Shuai Wang. Octfusion: Octree-based diffusion models for 3d shape generation. In *Computer Graphics Forum*, 2025. 2
- [106] Liying Yang, Chen Liu, Zhenwei Zhu, Ajian Liu, Hui Ma, Jian Nong, and Yanyan Liang. Not all frame features are equal: Video-to-4d generation via decoupling dynamic-static features. *arXiv:2502.08377*, 2025. 2
- [107] Xingyi Yang, Songhua Liu, and Xinchao Wang. Hash3d: Training-free acceleration for 3d generation. In *Computer Vision and Pattern Recognition*, 2025. 1
- [108] Zetong Yang, Yanan Sun, Shu Liu, Xiaojuan Qi, and Jiaya Jia. Cn: Channel normalization for point cloud recognition. In *European Conference on Computer Vision*, 2020. 4
- [109] Zhangsihao Yang, Mingyuan Zhou, Mengyi Shan, Bingbing Wen, Ziwei Xuan, Mitch Hill, Junjie Bai, Guo-Jun Qi, and Yalin Wang. Omnimotiongpt: Animal motion generation with limited data. In *Computer Vision and Pattern Recognition*, 2024. 6, 13
- [110] Chun-Han Yao, Yiming Xie, Vikram Voleti, Huaizu Jiang, and Varun Jampani. Sv4d 2.0: Enhancing spatio-temporal consistency in multi-view video diffusion for high-quality 4d generation. *arXiv:2503.16396*, 2025. 2
- [111] Hu Ye, Jun Zhang, Sibao Liu, Xiao Han, and Wei Yang. Ip-adapt: Text compatible image prompt adapter for text-to-image diffusion models. *arXiv:2308.06721*, 2023. 5
- [112] Xingyilang Yin, Xi Yang, Liangchen Liu, Nannan Wang, and Xinbo Gao. Point deformable network with enhanced normal embedding for point cloud analysis. In *AAAI Conference on Artificial Intelligence*, 2024. 4
- [113] Yuyang Yin, Dejjia Xu, Zhangyang Wang, Yao Zhao, and Yunchao Wei. 4dgen: Grounded 4d content generation with spatial-temporal consistency. *arXiv:2312.17225*, 2023. 2
- [114] Heng Yu, Chaoyang Wang, Peiye Zhuang, Willi Menapace, Aliaksandr Siarohin, Junli Cao, László Jeni, Sergey Tulyakov, and Hsin-Ying Lee. 4real: Towards photorealistic 4d scene generation via video diffusion models. *Neural Information Processing Systems*, 2024. 2
- [115] Biao Zhang, Jiapeng Tang, Matthias Niessner, and Peter Wonka. 3dshape2vecset: A 3d shape representation for neural fields and generative diffusion models. *Transactions On Graphics*, 2023. 2
- [116] Bowen Zhang, Sicheng Xu, Chuxin Wang, Jiaolong Yang, Feng Zhao, Dong Chen, and Baining Guo. Gaussian variation field diffusion for high-fidelity video-to-4d synthesis. In *International Conference on Computer Vision*, 2025. 1, 2, 3, 5, 6, 10, 13
- [117] Haiyu Zhang, Xinyuan Chen, Yaohui Wang, Xihui Liu, Yunhong Wang, and Yu Qiao. 4diffusion: Multi-view video

- diffusion model for 4d generation. *Advances in Neural Information Processing Systems*, 2024. 2
- [118] Hao Zhang, Haolan Xu, Chun Feng, Varun Jampani, and Narendra Ahuja. Physrig: Differentiable physics-based skinning and rigging framework for realistic articulated object modeling. *arXiv:2506.20936*, 2025. 3
- [119] Jiaxu Zhang, Shaoli Huang, Zhigang Tu, Xin Chen, Xiaohang Zhan, Gang Yu, and Ying Shan. Tapmo: Shape-aware motion generation of skeleton-free characters. *arXiv:2310.12678*, 2023. 3
- [120] Jiaxu Zhang, Shaoli Huang, Zhigang Tu, Xin Chen, Xiaohang Zhan, Gang Yu, and Ying Shan. Tapmo: Shape-aware motion generation of skeleton-free characters. In *International Conference on Learning Representations*, 2024. 5
- [121] Jia-Peng Zhang, Cheng-Feng Pu, Meng-Hao Guo, Yan-Pei Cao, and Shi-Min Hu. One model to rig them all: Diverse skeleton rigging with unorig. *Transactions on Graphics*, 2025. 2
- [122] Xinyi Zhang, Naiqi Li, and Angela Dai. Dnf: Unconditional 4d generation with dictionary-based neural fields. In *Computer Vision and Pattern Recognition*, 2025. 1, 2, 4, 12
- [123] Zibo Zhao, Wen Liu, Xin Chen, Xianfang Zeng, Rui Wang, Pei Cheng, Bin Fu, Tao Chen, Gang Yu, and Shenghua Gao. Michelangelo: Conditional 3d shape generation based on shape-image-text aligned latent representation. *Advances in neural information processing systems*, 2023. 2
- [124] Zibo Zhao, Zeqiang Lai, Qingxiang Lin, Yunfei Zhao, Haolin Liu, Shuhui Yang, Yifei Feng, Mingxin Yang, Sheng Zhang, Xianghui Yang, et al. Hunyuan3d 2.0: Scaling diffusion models for high resolution textured 3d assets generation. *arXiv:2501.12202*, 2025. 1, 2, 9
- [125] Xin-Yang Zheng, Hao Pan, Yu-Xiao Guo, Xin Tong, and Yang Liu. Mvd²: Efficient multiview 3d reconstruction for multiview diffusion. In *SIGGRAPH*, 2024. 2
- [126] Hanxin Zhu, Tianyu He, Xiqian Yu, Junliang Guo, Zhibo Chen, and Jiang Bian. Ar4d: Autoregressive 4d generation from monocular videos. *arXiv:2501.01722*, 2025. 2